Draft Manuscript for Review

The Skaergaard PGE and gold deposit: the result of in situ fractionation, sulphide saturation, and magma chamber-scale precious metal redistribution by immiscible Fe-rich melt

Journal:	*Journal of Petrology*
Manuscript ID:	JPET-Jul-14-0096.R1
Manuscript Type:	Original Manuscript
Date Submitted by the Author:	n/a
Complete List of Authors:	Nielsen, Troels; Geological Survey of Denmark and Greenland, Department of Economic Geology Andersen, Jens; University of Exeter, Camborne School of Mines Holness, Marian; University Of Cambridge, Keiding, Jakob; Geological Survey of Denmark and Greenland, Rudashevsky, Nikolay; CNT Instruments LLC, Rudashevsky, Vladimir; CNT Instruments LLC, Salmonsen, Lars-Peter; Aarhus Universitet, Institute for Geoscience Tegner, Christian; Aarhus Universitet, Institute for Geoscience Veksler, Ilya; GFZ, Inorganic and Isotope Geochemistry
Keyword:	Skaergaard intrusion, mineralisation, PGE, gold, magma chamber, immiscibility
Note: The following files were submitted by the author for peer review, but marked to be sent in Off-Line.	
Supplementary Data Appendix 3 Supplementary Data Appendix 2 Supplementary data Appendix 1	

INTRODUCTION

The layered gabbros of the Skaergaard intrusion in southern East Greenland (Wager & Brown, 1968; McBirney, 1996) host a major stratabound PGE and Au mineralisation (Bird *et al.*, 1991; Andersen *et al.*, 1998; Nielsen *et al*., 2005; Holwell & Keays, 2014). With a total metal content of >10 million ounces of gold and >30 million ounces of PGE, strongly dominated by palladium (Pd/Pt ~ 13, Nielsen *et al.*, 2005), the mineralisation represents a significant global PGE and Au resource. The hallmark of the Skaergaard-type mineralization (Miller & Andersen, 2002) is the presence of distinct and repeated PGE, Au and Cu enriched levels, with local and repeated fractionation of precious metal ratios (Nielsen, 2013). The structure of the mineralisation has been described as a 50m high set of gold-rimmed and perfectly concordant saucers defined by gabbro rich in Pd and Pt (Andersen *et al*., 1998; Nielsen *et al*., 2005). The saucers show upward decreasing diameter and near-constant, stratigraphic separation across the intrusion.

A variety of models has been put forward to explain the stratigraphic position, structure, mineralogical evolution, and precious metal geochemistry of the mineralisation (e.g. Bird *et al.*, 1991; Andersen *et al*., 1998, Nielsen *et al*., 2005, Andersen 2006; Holwell & Keays, 2014), but a detailed understanding of the mineralisation processes and their timing has remained elusive.

The most commonly accepted models for stratiform PGE deposits are based on the assumption of bulk liquid sulphide saturation and the formation of immiscible sulphide melt which, during descent, scavenges precious metals and accumulates to form reef-type deposits (see reviews in Naldrett, 2004; 2011; commonly referred to as “downers models”). Alternative models argue for upward migration of fluids and/or melts causing dissolution of already formed sulphides and re-deposition of precious metals in stratigraphic, mineralogical and/or geochemical traps

(Boudreau & McCallum, 1992; Meurer & Boudreau 1998; Meurer *et al.*, 1999; Boudreau & Meurer, 1999; commonly referred to as "uppers models"). A traditional sulphide saturation model would predict a continuum of precious metal fractionation, and not the observed multiple levels of PGE mineralisation with repetition of Pd/Pt ratios (Nielsen, 2013), and therefore cannot be applied to the Skaergaard mineralization (see also Holwell & Keays, 2014). Likewise, models that assume upward percolation and re-deposition of sulphides are not applicable to the Skaergaard, as the observed Pd, Pt, Au and Cu anomalies are broadly contemporaneous in gabbros in the floor (Andersen *et al*., 1998), the roof (Salmonsen & Tegner, 2013) and the walls (Nielsen, 2013).

In this paper, we draw together information from previous publications, survey and company reports in the public domain, and hitherto confidential or unpublished information. We present and interpret the petrography, the layering and crystallization processes in the host of the floor mineralisation, the overall fractionation of Pd, Pt and Au in bulk liquid, and the distribution of precious metals in the roof, walls and floor rocks. We establish the timing of mineralisation processes relative to the solidification of the hosts in floor, roof and walls. We also correlate and place time constraints on the evolution of silicate, sulphide, and metal melts in the intrusion.

The combined information and the use of the precious metals as tracers reveals that the crystallisation of the silicate host and mineralization processes in roof and floor were intimately related, dominated by *in situ* fractionation of silicate melt, and characterized by chamber-wide redistributions by the movement of immiscible silicate melts in a scenario that departs significantly from that generally assumed for the Skaergaard intrusion.

GEOLOGICAL SETTING OF THE SKAERGAARD INTRUSION

Shape and volume

The 56 Ma old Skaergaard intrusion (Wotzlau *et al.*, 2012) is a ~300 km^3 box-shaped layered gabbro body (~11 x 7 x 3.8 km) in the rifted volcanic margin of the North Atlantic Igneous Province (e.g. Wager & Deer, 1939; Wager & Brown, 1968; McBirney, 1996; Irvine *et al.*, 1998; Nielsen 2004; Svennevig & Guarneiri, 2012; Fig. 1). The intrusion is affected by syn-

and post-solidification faulting and dyke emplacement (e.g. Nielsen, 1978), and is presently tilted approximately 20º toward the south (Nielsen, 2014a).

The intrusion was filled by several pulses of magma (Holness *et al*., 2007; 2015), which were then homogenized (e.g. Salmonsen & Tegner, 2013) and crystallized under generally closed conditions. The bulk composition was that of an Fe-rich tholeiitic basalt (Wager & Brown, 1968). It crystallised inwards from the margins (onion structure: Nielsen, 2004a) and is divided in three series: the roof gabbros (Upper Border Series, UBS), the wall gabbros (the Marginal Border Series, MBS), and the floor gabbros (the Layered Series, LS, Fig. 1). The last floor cumulate to form was the Sandwich Horizon (SH) that separates ~3200m of floor gabbros (LS) from the overlying ~600m of roof (UBS) gabbros (average thicknesses from Nielsen (2004a)). The roof gabbros preserved near the south-eastern margin of the intrusion reach ~900m in thickness (Naslund, 1984; Salmonsen & Tegner, 2013). The wall gabbros thicken upward to a maximum >700 meters at the level of the Sandwich Horizon (Hoover, 1989; Nielsen, 2004a; Holness *et al.*, 2011).

Phase layering and subdivisions

These three series are further subdivided into zones and sub-zones on the basis of liquidus mineral assemblages (Wager & Brown, 1968). The most primitive floor cumulates (the Hidden Zone and Lower Zone, LZ) have liquidus plagioclase and olivine (Lower Zone a, LZa), clinopyroxene joins in LZb, with the addition of magnetite and ilmenite in LZc. Re-crystallisation of the Fe-Ti oxides obscures the exact timing of their arrival on the liquidus. Middle Zone (MZ) has no olivine on the liquidus, with the liquidus assemblage comprising plagioclase, clinopyroxene, ilmenite, titanomagnetite and (sporadically) low-Ca pyroxene (pigeonite). Upper Zone (UZ) has plagioclase, clinopyroxene, ilmenite, Ti-magnetite, and Fe-rich olivine in UZa, joined by apatite in UZb, and by ferrobustamite in UZc. (Fig.1c). Significant, irregularly shaped, volumes of melanogranophyre, often forming interconnected sill-like bodies, comprise up to 30

vol. % of the uppermost parts of UZb and UZc. Salmonsen *et al*. (2014) report significant volumes of cognate granophyre in roof rocks above the Sandwich Horizon.

The evolution of the liquidus mineralogy in the roof (Salmonsen & Tegner, 2013; Fig. 1) and the wall gabbros (Hoover, 1989) parallels the evolution of the floor (e.g. McBirney, 1989), providing an opportunity to evaluate the sub-liquidus evolution of the same bulk liquid in three contrasting gravitational regimes (e.g. McBirney & Nicolas, 1997; Boudreau & McBirney, 1997). Following tradition, we refer to all Skaergaard cumulates as "gabbros" despite the fact that plagioclase contains <50% An above MZ and in equivalent gabbros of UBS and MBS (e.g. Wager & Brown, 1968; Hoover, 1989; Salmonsen & Tegner, 2013; Namur *et al.*, 2014). Strictly, these rocks are ferrodiorites.

Setting and structure of Triple Group and the floor mineralisation

The Skaergaard PGE-Au mineralisation is located in the lower part of the stratigraphic interval referred to as the Triple Group, comprising the upper 100 m of Middle Zone (MZ, Fig. 1; Andersen *et al.*, 1998). The Triple Group is a succession of gabbros characterised by large-scale macrorhythmic layering including three distinct leucogabbro layers, L1, L2 and L3 (see Andersen *et al.* (1998) for details). The leucogabbro layers are 5-7m thick and overlain by layers of melanogabbro (termed M-layers) followed by meso- or average-gabbros to the base of the next leuco-gabbro layer. A buff coloured layer 20m below L1 has been accepted as a fourth Triple Group member and is referred to as L0. Although it is not as thick or as plagioclase-rich as L1, L2 and L3 (Andersen *et al.,* 1998), it is compositionally distinct from the overlying macrorhythmic layering (and clearly distinguishable on the basis of specific gravity, Andersen *et al*. (1998)). It is the stratigraphic marker for the main Pd+Pt mineralisation.

The saucer structure of the mineralisation described by Andersen *et al*. (1998) and Nielsen *et al*. (2005) was discarded by Holwell & Keays (2014), who instead suggest a structure involving an increasing stratigraphic separation between a lower Pd zone and discordant Au and Cu zones rising high over the Pd zone in the centre of the mineralization, and the formation of additional

discordant mineralization levels in an intermediate zone. Because a robust structural framework is essential for data presentation and modelling, we re-iterate the evidence supporting the saucer model in this contribution.

Lithological correlation of Triple Group

The lithological stratification in Triple Group is easily correlated across the intrusion in the field and in specific gravity profiles obtained from 13 drill cores (Appendix 1). The drill core profiles have been corrected for structural disturbances at faults and dykes. Illustration of the correlations cannot be accommodated on a printed page without losing most of the critical details and the reader is invited to inspect Appendix 1, which also provides data on the internal separation between L-layers. The stratigraphy of the Triple Group is remarkably constant across the intrusion (Appendix 1). Typically ~13 m of layered gabbro separate L0 and L1, ~10 m separate L1 and L2, and ~62 m separate L2 and L3.

Shape of Triple Group

The Triple Group forms a broad bowl-like structure (Fig. 1) with a central depression of >500m (Fig. 1; Nielsen, 2004a; Nielsen *et al.*, 2009; Svennevig & Guaneiri, 2012). The bowl shape is reconstructed in more detail from drill core logs (Turner, 1990; Watts, Griffis & McOuat Ltd., 1991) in a projection of the top of L3 (UZ-MZ boundary) onto an almost E-W oriented plane perpendicular to the regional dip (Appendix 2). The Triple Group correlations show that in the centre of the intrusion the top of L3 is ~700m lower than at the sides (Appendix 2).

Correlations of Pd, Pt and Au in the floor mineralization

The mineralisation levels in the floor can be correlated between >40 drill cores and 20 chip lines (data in Watts, Griffis & McOuat Ltd. (1991), Turner (1990), Bernstein & Nielsen (2004), and in Appendix 3). The individual Pd mineralisation levels along the floor were numbered by Platinova during the original exploration (on the basis of metre-intervals of chip lines and cores)

from the top and downwards as Pd1 to Pd5 (Fig. 2.; Andersen *et al.*, 1998; Nielsen *et al.*, 2005). The Pd2, Pd3 and Pd4 levels are further subdivided into characteristic a- and b-levels (Fig. 2; Nielsen, 2001).

In core 90-23A (Figs. 1 and 2, Appendix 3), from near the east margin of the intrusion, only the lowermost mineralisation levels reach concentrations of economic interest. Nevertheless, all Pd levels can be identified across the intrusion and are stepwise enriched in Pd+Pt toward the centre of the mineralization (Appendix 3; Andersen *et al.,* 1998). As above, the correlation between 13 geochemical profiles, corrected for structural disturbances at faults and dykes, cannot be shown in print without loss of critical detail, but can be examined in Appendix 3. Within the limits of resolution, the Pd levels maintain near-constant stratigraphic separation of ~10m between Pd5, Pd4a, Pd3a, Pd2a and Pd1 across the intrusion (Appendix 3).

Irrespective of how many levels the Pd occupies, the Au is invariably found in the uppermost level of Pd enrichment. At the margin of the intrusion Au is found in the Pd4 level (drill core 90-23A, Fig. 2b), a position which shifts to Pd3, and then Pd2 and Pd1 toward the geometric centre of the mineralisation layers. In addition, a gold-only level (below referred to as UAuM), with more than trace concentrations of Pd, may be present as much as 14m above the uppermost Pd level (Appendix 3). In the stratigraphic interval from Pd1 to Pd5, and within the resolution of the assays (1m average samples and +/- 1m in depth in the core), elevated Au invariably coincides with the Pd levels Pd4 to Pd2 (Fig. 2). With the exception of the gold-only level, Au is always found at the tightly and stratigraphically controlled Pd levels (tabulated in Appendix 3).

Correlation between mineralization and host rock lithologies

The correlation between mineralization levels and layering of the host gabbros is established by the stratigraphic relationship between Pd+Pt in the Pd5 level and L0 (Andersen *et al*., 1998), and by the location of Pd1 to Pd5 in the specific gravity profile in drill core 90-22 (Bernstein & Nielsen (2004); Appendix 4). The Pd+Pt peak of Pd5 is invariably located 1-2m

below the gravity minimum in the L0 layer (Appendix 5). In drill core 90-22, the mineralization levels invariably occur in sections of the stratigraphy characterized by upwards-decreasing density (Fig. 3, based on data in Appendix 4).

Established structure of the floor mineralisation.

The combination of the correlation of the lithological stratigraphy across the intrusion floor (Appendix 1), the bowl shape of the floor (Appendix 2), the correlations of Pd levels across the floor (Appendix 3), and the correlation between the mineralisation and lithological layering (Appendix 5), results in the saucer structure depicted in Figure 4 and presented by Andersen *et al*. (1998), Nielsen (2001) and Nielsen *et al.* (2005). The structure of the mineralisation is, as originally argued by Andersen *et al*. (1998), best described as a set of gold-rimmed saucers of upward decreasing radius. A summary of the internal separation between leucogabbro layers L0 to L3 and Pd-levels 1 to 5 as well as the separation between L1 and Pd5 is shown in Table 1.

Appendices 1-3 and 5 document in full the detailed modal and geochemical variations that define the structure. The saucer structure established in Andersen *et al*. (1998) is a robust framework for the data presentation, the development of constraints for the modelling, and for our mineralisation model.

SAMPLES AND METHODS

Samples were collected from Platinova drill cores (drilled in 1989-1991, a selection of which is now stored at the Geological Museum in Copenhagen) as well as during scientific field campaigns in the period 1990-2011. Different analytical methods have been used on these samples and are summarised in the primary publications. In general, mineral compositions were determined by electron-probe microanalysis using wavelength dispersive spectrometers (Andersen, 1996; Thy *et al.,* 2009); whole-rock major element concentrations by XRF (fused disks, method by Kystol & Larsen, 1999; Salmonsen & Tegner, 2013); trace element concentrations by XRF (pressed powder pellets), ICP-OES and ICP-MS (four acid digestion); and

Pd, Pt, and Au by ICP-MS after pre-concentration in a Pb-sulphide bead. Detection limits are 1 ppb for Au and 0.1 ppb for Pd and Pt (Bernstein & Nielsen, 2004). Fe_2O_3 and FeO were measured by dissolution and titration (Kystol & Larsen, 1999).

Relative volumes of lithological units of the floor cumulates (Nielsen, 2004a), and the relative stratigraphic thickness at the roof and walls, form the basis for calculations of the progress of solidification, expressed as the fraction of liquid remaining (*F*), and the liquid line of descent. Mineral abundances in host rocks are determined using CIPW norms using measured Fe_2O_3 and FeO (Appendix 4). The norms correspond well with modes calculated by Thy *et al.* (2009) (Appendix 9).

As the FeTi-oxides have re-equilibrated to lower temperature, their normative abundances are not representative of the liquidus proportions of ilmenite and titanomagnetite. Liquidus titanomagnetite ($TiMt_{24}$) contains c. 24 wt% TiO_2 (Thy *et al*., 2006) and the actual amount of titanomagnetite that crystallised from the bulk liquid is calculated by adding an amount of ilmenite (with 52% TiO_2) to the calculated normative abundance of titanomagnetite in the proportions 0.82 part ilmenite to 1 part magnetite . The remaining normative ilmenite (ilm_{24}) approximates the primary proportion of liquidus ilmenite. Correlations between calculated primary $TiMt_{24}$ and vanadium (Appendix 9) and between ilm_{24} and niobium (Appendix 9) validate these approximations.

NEW AND COMPILED INFORMATION

Petrographic observations

Host rock parageneses

The Middle Zone gabbros have been described in great detail in previous publications (e.g. Holness *et al.,* 2011; Namur *et al.,* 2014 and references therein). The liquidus paragenesis of the bulk liquid from which MZ gabbros formed (P1) includes plagioclase, clinopyroxene, low-Ca pyroxene (?), ilmenite, and spinel (titanomagnetite) (e.g. Thy *et al.*, 2006). FeTi-oxides have been significantly affected by recrystallization, and the only preserved primary FeTi-oxides are ~1mm,

disseminated, euhedral ilmenite crystals (see below). Titaniferous magnetite crystals grown as part of P1 are present, but exceedingly rare (Bollingberg, 1995). Liquidus minerals of P1 systematically evolve upwards toward lower temperature compositions without compositional reversals (Thy *et al*., 2009).

In addition to the liquidus paragenesis, Nielsen & Bernstein (2009), Holness *et al*. (2011) and Humphreys *et al*. (2011) identify a distinct paragenesis (P2) of symplectites and reaction rims related to anhedral masses of FeTi-oxide. This P2 paragenesis comprises: olivine, clinopyroxene, and high An-plagioclase apatite, and FeTi-oxides. The P2 paragenesis has been attributed to the selective loss of a buoyant Si-rich immiscible conjugate from the mush, leaving behind a reactive immiscible Fe-rich interstitial melt (Holness *et al.,* 2011). We present backscatter images from the stratigraphic interval of the floor mineralisation (Fig. 5) to illustrate and further evaluate the petrographic relations of FeTi-oxides, and the possible importance of immiscibility between Fe-rich and Si-rich liquids in the evolution of the bulk liquid (e.g. Jakobsen *et al*., 2005; 2011), both during the crystallisation of the host rocks of the mineralization (Holness *et al.,* 2011; Humphreys *et al.,* 2011), and during the formation of the mineralization (Nielsen & Bernstein, 2009; Holwell & Keays, 2014).

Anhedral FeTi-oxide grains (Fig. 5a) are separated from all other mineral phases by rims of olivine and/or orthopyroxene, irrespective of the composition of the adjacent phase. In Fig. 5b resorbed clinopyroxene floats in a sea of olivine, a phase that should not be on the liquidus at upper MZ times. In Fig. 5c olivine-orthopyroxene rims separate grains of FeTi-oxides and plagioclase, with the latter partially replaced by symplectite. Some plagioclase crystals are apparently intruded by thin apophyses of titano-magnetite with related symplectitic intergrowth (Fig. 5d), presumably crystallised from a late silicate melt. Euhedral apatite crystals (Fig. 5e) are found in anhedral, intergrowths of ilmenite and magnetite. Finally, ilmenite grains commonly host perfectly rounded poly-mineralic inclusions dominated by amphibole and hydrous silicates (Fig. 5f). The inclusions are described in more detail by Godel *et al*. (2014).

In agreement with Nielsen & Bernstein (2009), Holness *et al*. (2011) and Humphreys *et al*. (2011), we suggest that the petrographic features shown in Fig. 5, and the recrystallization of clinopyroxene to mozaics of small clinopyroxene grains (Fig. 6), point to the crystallization of a significant volume of the Triple Group gabbros from a melt that was out of equilibrium with the P1 paragenesis. The boundary between P1 and P2 parageneses can be traced along resorbed margins of P1 plagioclase and pyroxene (Fig. 6) permitting the identification of regions containing the P2 paragenesis. These regions also contain all the anhedral FeTi-oxide masses, which can therefore be assigned to the P2 paragenesis. Further evidence that most of the FeTi-oxides in the gabbros formed during late-stage crystallisation in the crystal mush is provided by the grains of euhedral apatite which they enclose, together with a proportion of normative titanomagnetite (see below) significantly in excess of that expected of the modal proportion in the liquidus paragenesis of Skaergaard liquid at upper MZ times (Thy *et al.,* 2006).

The tracing of the boundary between P1 and P2 (Fig. 6) suggests that the late P2 paragenesis can constitute as much as half the volume of the gabbros hosting the floor mineralisation.

Sulphides and precious metal parageneses

Petrographic observations for sulphide and precious metal assemblages and parageneses in the floor mineralisation are reported by Andersen *et al.* (1998), Cabri (2004), Nielsen *et al.* (2005), Godel *et al.* (2014), and Rudashevsky *et al*. (2014, 2015), and in greater detail in mineralogical survey reports (Nielsen *et al.* (2003a-e), Rudashevsky & Rudashevsky (2005a-b; 2006a-b), and Rudashevsky *et al.* (2004; 2009a-b; 2010a-d; 2012a-i; 2013a-b)). In the mineralogical reports (for which all references can be found in Appendix 12), mineralogical, chemical and paragenetic information is provided for >1500 sulphide and >4000 precious metal grains from the different levels throughout the mineralization. The mineralogical studies described in the reports were based on monolayer samples of concentrates obtained by careful grain separation (methods are described by Rudashevsky *et al*., 2004). The method used ensures a high and representative

recovery of sulphide and precious metal grains (several hundred grains in 1kg samples with Pd+Pt at the ppm level) and a sufficient basis for a reliable determination of the precious metal and sulphide parageneses and assemblages.

At very low concentrations, sulphide takes the form of crystallised droplets in P1 ilmenite grains (Godel *et al.,* 2014; Fig. 7a) and in P1 grains of titaniferous magnetite and clinopyroxene, as well as forming irregularly shaped grains on the boundaries between other rock-forming minerals. The sulphides are entirely dominated by bornite and chalcocite (e.g. Bird *et al.,* 1991; Nielsen *et al.,* 2005; Rudashevsky *et al*., 2004; McDonald *et al*., 2009; Appendix 12) and contain concentrations of precious metals lower than the detection limit for electron microprobe analysis. Discrete grains of Fe-rich sulphides (e.g. chalcopyrite) are rare and occur only as exsolutions in Cu-rich sulphide or as the result of late alteration of bornite-rich assemblages, e.g. in roof gabbros. Solidified sulphide droplets and grains, as well as precious metal phases, are disseminated throughout the floor mineralization and show no clear indication of local accumulation, most likely because the grains were too small to sink. Crystals of FeTi-oxides with a density similar to that of the sulphide melt droplets did apparently not sink. Droplets enclosed in other phases, e.g. ilmenite (Godel *et al.,* 2014), were protected from later reactions with silicate melt, as opposed to irregular blebs of sulphide between matrix grains.

In the centre of the intrusion, the precious metal mineral paragenesis is strongly dominated by skaergaardite (PdCu, Fig. 7b-e) together with a paragenesis of (Pd, Pt, Au, Cu) alloys, of arsenides and sulphides (not illustrated), and tetra-auricupride (AuCu, Fig. 7f-g) with their abundance increasing in proportion upward through the stratigraphy (see mineralogical reports in Appendix 12). In Pd5, 94-95% by volume of Pd-bearing grains (a total of 368 PGM grains identified) is skaergaardite (PdCu, Nielsen *et al*., 2003b; Appendix 12). Skaergaardite forms rounded (Fig. 7e) droplet-like to anhedral grains as well as euhedral crystals within rounded sulphide grains interpreted as crystallised droplets (Fig. 7b). Skaergaardite may be attached to Cu-

sulphide at host rock grain boundaries, or form euhedral to anhedral grains free of any association with sulphide in the matrix of the gabbros.

In contrast, the parageneses in Pd5 and Pd4 in drill cores from the margins of the intrusion are more mineralogically diverse. Inter-metallic alloys are dominated by zvyagintsevite (Pd_3Pb, Fig. 7h-i) which decreases from 73 in Pd5 to 24 vol. % in Pd4 (in Appendix 12: Nielsen *et al.,* 2003a,d,e; 2005; Rudashevsky *et al.,* 2009b), while arsenides, sulphides and gold minerals (e.g. bogdanovite, $(Au,Pd,Pt)_3(Cu,Fe)$) and Au-rich intermetallic alloys (AuCu and Au_3Cu) increase in importance up the stratigraphy. The maximum concentration of 2000ppb Au in Pd4a in drill core 90-23A compares to a maximum of only 50-150ppb Au in Pd4 in the same mineralisation level in central drill cores (Fig. 2a).

A remarkable feature of the paragenesis is the presence of Cu-sulphide grains containing rounded PGE-rich particles comprising a complex amalgam of Cu-sulphide and skaergaardite (PdCu) (Figs. 7j, k). These rounded particles are surrounded by a meniscus and, following Rudashevsky *et al.* (2015), we interpret them as solidified immiscible droplets of precious metal melts inside Cu-sulphide melt: they illustrate the coexistence of Cu-rich sulphide and low-S metal melts as shown by the experiments of Karup-Moller & Makovicky (1999).

Grab sample Cu, Pd, Pt, and Au profiles in floor, roof, and walls gabbros

The whole-rock variations of Cu concentration in the floor (LS, data from Salmonsen & Tegner (2013)), roof (UBS, data from Salmonsen & Tegner (2013)), and wall gabbros (MBS, Appendix 6) can be compared using the calculated proportions of residual liquid (*F*, where *F* is determined by stratigraphy in MBS and UBS; and as a mass proportion in LS (Nielsen, 2004). In all three settings the elevated Cu concentration is observed after crystallization of ~¾ of the Skaergaard magma (Fig. 8). Although the sample resolution is limited in UBS and MBS, and the absolute concentrations are very different, the general trends are the same in all three environments. As also concluded by Salmonsen & Tegner (2013), we observe a near-contemporaneous accumulation of Cu from a homogenized body of magma.

The stratigraphic variation of Pd, Pt and Au concentrations in LS, UBS and MBS is shown in Figs. 9, 10 and 11. Below the floor mineralization, the evolution of Pd and Pt in the grab sample profile divides into three stages (Fig. 9, Appendix 7): (1) Pd+Pt decreases from the base of LZa to upper LZb; (2) higher but variable Pd+Pt and Pd/Pt characterize the stratigraphic interval from upper LZb to Middle MZ; and (3) a zone of low PGE concentration (low-PGE-zone) defines the ~50m of stratigraphy below the floor mineralization (see Appendix 11, data from drill core 90-10). Both below and above the mineralisation (Fig. 10a), the Pd/Pt ratios are limited to values of ~3 + (Pd/10), where 3 is the Pd/Pt of bulk Skaergaard liquid (see Fig. 15) and 10 is an approximation of the maximum solubility of Pt in basaltic melt (c.f. Farges *et al.,* 1999). The apparently high Pd/Pt value of 47 in one sample may be an error due to a very low Pt concentration of 1 ppb.

In the grab sample profile, the mineralised interval shows two contrasting trends of variability: the first, which displays high Pd+Pt (~4 ppm) and moderate Pd/Pt (~15) is confined to the interval from 10m below Pd5 to the top of Pd4 (excluding peak Pd4b); while the second has moderate Pd+Pt (~1.2 ppm) and high Pd/Pt (>60) and includes the remainder of the floor mineralisation. Neither of these trends in precious metal concentration has similarities with the variations either below or above the mineralisation (Fig. 10b) - this implies that the processes that controlled the accumulation of PGE in the floor mineralisation were only operative during a short interlude at upper MZ times. A detailed description of the systematics of (Pd+Pt) and Pd/Pt variations in the mineralised horizons requires a higher sample resolution than is possible with the grab sample profile. Such a sample resolution can be obtained from drill core 90-22 (Fig. 12, Appendix 4) and is described and discussed in detail below.

As in the floor, anomalies in Pd, Pt and Au are found near the Cu anomaly in both roof and wall gabbros (Table 2, Fig. 11), but the PGE and Au concentrations are at least an order of magnitude lower. In the floor, Pd, Pt and Au anomalies occur below the Cu anomaly (Fig. 2a), whereas all the anomalies coincide in the roof gabbros (Fig. 11a). In wall gabbros the PGE, Au and Cu peaks occur progressively inward in the order of *D*-values Pd>Pt>Au>Cu (Fig. 11b).

While the mineralisation processes appear to be broadly contemporaneous in floor, roof and walls, these differences place significant constraints on any mineralisation and crystallisation models.

High-resolution chemical stratigraphy and subdivision of the floor mineralisation

Detailed compositional variations through the floor mineralisation can be obtained from the continuum of 25-cm samples in drill core 90-22 (259 samples in total, full data in Bernstein & Nielsen (2004); Appendix 4). The data set includes bulk rock major and trace element analyses, Pd, Pt, and Au determinations, density measurements, and CIPW norms. The data is used for Figures 12-19, 21 and 23. Here we only provide general compositional characteristics for the mineralisation, including correlations between Cu and Pd, Pt and Au (Fig. 12), and variations in Pd+Pt and Pd/Pt: these are used to subdivide the mineralisation (Fig. 13).

Whole rock Cu, Pd, Pt and Au in floor mineralization

The variation in Pd, Pt and Au relative to Cu falls into four, compositionally distinct, suites (Fig. 12a-c, Appendix 4). Suite 1 comprises Pd5 as well as the samples from the "subzone" below Pd5 to the top of Pd3, together with the Pd2 mineralisation level. Suite 1 is characterised by distinct enrichments in precious metal concentrations, but with no observable correlation with Cu (up to >3 ppm PGE and 80 – 150 ppm Cu). Suite 2 includes samples between mineralisation levels Pd3, Pd2 and Pd1, and is characterised by low concentrations of Cu and precious metals (PM). Suite 3 includes the Au-rich levels in the upper part of the precious metal mineralisation, and can be divided into two: Pd1 itself; and an overlying Pd-poor Au level. Suite 4 includes the Cu-rich mineralisation levels that contain near-constant precious metal to Cu ratios (e.g. Cu/Pd~11,000; Cu/Pt ~70,000; and Cu/Au ~7,000).

Combined, the four suites point to a common composition (CC) with ~150 ppm Cu (max.), ~13 ppb Pd, ~1.3 ppb Pt, ~10 ppb Au, a Pd/Pt of ~10, and an Au/Pd of ~0.8 and an Au/Pt of ~8. We consider the elemental ratios of this common composition to be representative of the bulk mineralisation prior to internal fractionation and remobilisation of precious metals. These ratios

for the primary bulk mineralisation are confirmed by independent modelling (see the section below on modelling of LLD for precious metals).

Stratigraphic subdivision of the floor mineralisation

Total PGE and Pd/Pt (Appendix 4, Fig. 13a) increase steadily upwards from the low-PGE-zone from 200 ppb and 5-6, respectively, to >500 ppb and 10 at the base of Pd5. This section of the stratigraphy was referred to as the "subzone" by Holwell & Keays (2014), and here as the Pd6 level (to be consistent with the established naming of Pd levels as Pd1 to Pd5 (Nielsen *et al.* (2005)). The mineralisation peak in Pd5 reaches 3 ppm Pd+Pt with a Pd/Pt of 25 (Figs. 13a, b), and concentrations subsequently decline to <1 ppm PGE with Pd/Pt returning to 10 above the Pd5 peak, equivalent to the ratio below this excursion. Upwards the Pd/Pt increases to 20 in the lower 1m of L0 (Fig. 13a), to ~60 in a low-concentration Pd4b anomaly 5m above the Pd5 peak (Appendices 3 and 4) and to an average of ~13 in the Pd4a level. The Pd4b anomaly is often only identified by its Pd/Pt ratio, due to the absence of a marked increase in the concentration of Pd+Pt. With the exception of the Pd4b anomaly, Pd/Pt shows a general upwards increase through mineralisation levels Pd6 to Pd4.

The Pd/Pt evolution in the overlying Pd3, Pd2 and Pd1 levels is reversed (Fig. 13), with a ratio of up to 100 at the base of Pd3b, and systematic decreases in Pd/Pt both within and between the Pd levels. The variation within each of these levels is shown in Fig. 13b, in which it is clear that Pd/Pt attains the highest values in the basal parts of each of the Pd levels Pd1 to Pd3. Gabbros between the mineralisation levels show a general decrease in maximum PGE concentrations from ~300 to 200 ppb through Pd3 and Pd2, and from ~60 to 10 ppb through Pd2 and Pd1. We interpret this as a record of the exhaustion of Pd+Pt in the residual mush zone magma during the formation of Pd3 to Pd1.

The Au and Cu levels overlying the Pd-rich part of the mineralisation have no basal high Pd/Pt. In these levels, the Pd/Pt decreases to <5 as the Pd+Pt concentrations decrease below the

limit of detection (Fig. 9; Andersen *et al.,* 1998; Bernstein & Nielsen, 2004; Holwell & Keays, 2014; Keays & Tegner, 2013).

In summary, the P+Pt, Au, Cu and Pd/Pt variations divide the mineralisation into 4 sections (Fig. 13b): (1) the Lower PGE Mineralisation (LPGEM) with increasing Pd/Pt (5-13), comprising Pd6, Pd5 and Pd4 (with Pd4b as an exception, see below) and with all samples in Suite 1 in Fig. 12; (2); the Upper PGE Mineralisation (UPGEM), with decreasing Pd/Pt and comprising Pd3-Pd1. With increasing stratigraphic height, UPGEM is increasingly restricted to the central parts of the mineralisation (see saucer model, Fig. 4). The mineralisation levels of UPGEM belong to Suite 1, while gabbros between the mineralisation levels belong to Suite 2. UPGEM also includes the Au-enriched Pd1 that is found slightly above Suite 1 in Fig. 12); (3) the Upper Au-rich Mineralisation (UAuM) occurs at an unconstrained elevation above the highest Pd level. UAuM contains only trace concentrations of PGE and its own suite of Au-rich minerals (Au-rich Suite 3 in Fig. 12). The final section, (4), comprises the Cu-rich mineralisation levels (Suite 4 in Fig. 12) (CuM) that occur stratigraphically above the Pd levels, with more than trace concentrations of PGE.

Liquidus versus normative plagioclase compositions - timing of the mineralisation processes

Critical for the development of a mineralisation model is a correct timing of crystallisation and mineralisation events. The compositions of plagioclase cores offer the possibility for a correlation between petrographic and geochemical events and the evolution of the coexisting silicate liquid. When compared to normative bulk plagioclase compositions, the measured plagioclase core compositions evolve systematically across the mineralisation in the LS, MBS and UBS (Fig. 14, data in Appendix 8). The compilation of core compositions (Fig. 14) shows a decrease from An_{48-49} to An_{45-46} through the mineralisation in roof and walls. In the floor rocks the corresponding normative plagioclase compositions are anorthite-rich, but evolve in parallel with plagioclase in roof and wall rocks.

The plagioclase cores in the gabbros hosting the mineralisation in the floor rocks fall in the compositional window An_{44-46} (Fig. 14), somewhat less anorthitic than the composition An_{47} expected to have crystallised from the contemporary bulk magma at $F = 0.26$ (Table 4). In contrast to the plagioclase in the samples at the roof and walls in which the Pd mineralisation event is recorded (as high Pd/Pt), the floor plagioclase appears to have formed in melt that was evolved relative to the contemporary bulk melt. However, as we will argue below, this discrepancy is not the result of a delay in the timing of the floor mineralisation, but a consequence of differences in the relative timing of crystallisation of liquidus plagioclase and sulphide saturation in the mushy boundary layers (see section on the LLD of bulk liquid).

Figure 14 also shows the core compositions of liquidus plagioclase and the corresponding normative plagioclase composition for modelled bulk liquids between UZa and middle LZc (data and sources in Appendix 8). The bulk liquid trend is parallel to those of the roof, walls and floor. The floor and roof trends are complementary, with that of the bulk liquid being intermediate - as would be expected for a closed magma chamber. In addition, the bulk liquid trend (BL, Fig. 14) lies closer to that of the floor, as would be expected since 2/3 of the gabbros formed on the chamber floor, while only 1/3 formed at the roof and walls (Nielsen, 2004a).

FURTHER CONSTRAINTS REQUIRED FOR A MINERALISATION MODEL

The structure of the mineralisation is only one of the fundamental constraints required to develop a robust mineralisation model. We also need to know the bulk composition of the floor mineralisation, together with a well-constrained line of liquid descent (LLD) for Pd, Pt and Au, in order to deduce Pd, Pt and Au concentrations at the initiation of the mineralisation processes. We need to understand the processes that formed the layering that hosts the floor mineralisation, together with the relative timing of processes such as sulphide saturation and silicate-silicate liquid immiscibility at the floor, roof and walls. This relative timing can be used as a guide to the relative

timing of the same processes during *in situ* fractionation of the liquid in the mush zones of the magma chamber (e.g. Namur *et al*., 2014).

Bulk composition of the floor mineralisation (drill core 90-22)

We assume the high-resolution data from drill core 90-22 to be representative of the floor mineralisation in central drill cores. We define the floor mineralisation in drill cores from the centre of the intrusion using a minimum of 0.6 ppm PGE (= Pd+Pt) cut-off at the base and a 0.5 ppm Au cut-off at the top (Fig. 13a). Below the mineralisation, Pd+Pt decreases rapidly into the low-PGE-zone, while Au decreases rapidly to low concentrations above the mineralisation.

The average concentration of precious metals up through ~50m of stratigraphy is ~0.6 ppm total PGE (=Pd+Pt) and 0.15 ppm Au, with a Pd/Pt ratio of ~13 and an Au/Pd ratio of 0.25 (Appendix 4). In Pd5, the main Pd+Pt mineralisation level, Pd/Pt is ~10 and Au/Pd 0.04, whereas the equivalent ratios for the mineralisation above Pd5 are ~19 and 0.42 (the average for levels Pd4 to Pd1), respectively. The increase in *both* Pd/Pt and Au/Pd is unexpected (Nielsen, 2013; Holwell & Keays, 2014) as the relatively magnitude of the distribution coefficients for Pd, Pt and Au between Cu-sulphide and silicate liquid are generally accepted to be in the order Pd>Pt>Au (e.g. Makovicky, 2002; Naldrett, 2004; 2011).

PGE and Au in bulk liquids of the Skaergaard intrusion

The LLD of the Skaergaard bulk liquid is contentious (see Jakobsen *et al*. (2005) for a review of the significant differences between suggested LLDs). Nielsen *et al*. (2009) used a mass balance approach, based on a structural reconstruction of the intrusion (Nielsen, 2004a), that results in an initial bulk liquid with major element (and selected trace element) concentrations similar to those of contemporaneous plateau basalts (Momme *et al.*, 2002; Nielsen, 2004a; Jakobsen *et al*., 2005). The modelled LLD parallels that of Toplis & Carrol (1995), and shows CIPW norms of the liquids consistent with the modal composition of the gabbros (Appendix 10).

We use the Nielsen (2004) mass balance model to calculate the LLD for Pd, Pt and Au (Appendix 11).

The modelling is based on Pd, Pt and Au concentrations (Nielsen, 2004b), a suite of samples known as the Bollingberg profile (Bollingberg 1995); together with the average composition for the mineralisation (Appendix 4), and the mass proportions of zones and subzones in the intrusion provided by Nielsen (2004a). The sum of the Pd, Pt and Au content in all zones, subzones, and stratigraphic intervals in the intrusion provides a bulk composition for these elements in the intrusion (Fig. 15, Table 3). This bulk composition is characterised by Pd/Pt and Au/Pt ratios that are broadly similar to those of contemporaneous basaltic melts with appropriate Mg# numbers between 40 and 50 (Fig. 15a, Table 3).

The calculated LLD suggests that both Pd/Pt and Au/Pt increase in the bulk magma until the mineralisation event (Fig. 15a). This would be consistent with a predominant control by the progressive loss of Pt (most likely in the form of ferroplatinum), which has limited solubility in basaltic melt (~10ppb, Farges *et al*., 1999; Ertel *et al*., 2008; Bezmen *et al*., 2008). The rate of increase in Pd/Pt in bulk liquid is relatively slow in the stratigraphic interval between LZc to the base of the low-PGE-zone. This is not due to the onset of the mineralisation processes (see Fig. 10), but is most likely caused by local sulphide saturation and a minor loss of Pd by the local formation of small quantities of immiscible sulphide melts (Figs. 9, 10, 15a) during *in situ* fractionation (*sensu* Langmuir, 1989) in the mush zone. The local deposition of sulphide in LZc and MZ had little impact on the evolution of precious metal content in the bulk magma.

In the low–PGE-zone (Z to BM in Figs. 15a, b, c) compositions are also controlled only by loss of Pt. The Pd/Pt ratio is high in the mineralisation (~13; Fig. 15a; Appendix 11) compared to that of the contemporaneous bulk liquid (~6, Figs. 13a, 15a; Appendix 11), consistent with the generally accepted order of distribution coefficients Pd>Pt (e.g. Naldrett, 2004; 2011). Complementary and low Pd/Pt ratios characterize gabbros above the mineralisation (Fig. 15a).

Figures 15b and c show the LLD, the bulk assays of the mineralisation in all Platinova drill cores containing the entire mineralisation interval, together with the average bulk composition of the low-PGE zone (data in Appendix 11). The bulk assays of mineralisation intervals in the drill cores define a trend controlled by loss of Au and minor loss of Pt (Fig. 15c). The intersection between this trend and the line defined by the bulk composition of the low-PGE-zone and the contemporary bulk liquid composition (Z in Figs. 15b and c) identifies the composition of a sulphide melt prior to loss of Au and Pt. Such a melt had a Pd/Pt of ~9 and an Au/Pt of ~7 (Figs. 15b and c). The composition is almost identical to the independently established CC composition (Fig. 12), with a Pd/Pt of ~10 and an Au/Pt of ~8. We suggest that the process by which precious metals were delivered to the floor mush was constrained by these ratios.

The preserved floor mineralisation has a bulk composition with Pd/Pt of ~13 and an Au/Pd ratio of ~0.25 (Appendix 4, Fig. 15a). The ratios between the precious metals supplied to the chamber floor (CC in Figs. 12, 15b, c) were modified by the loss of Au and Pt, reducing Au/Pd from ~0.8 to ~0.25 and increasing Pd/Pt from ~10 to ~13 (Fig. 15, data in Appendix 11). This loss of Au and Pt is modelled in Figures 15b and c. The join between the complementary low-PGE-zone and the first-formed sulphide droplets with a Pd/Pt of 9 (shown by the orange dot in Figs. 15b and c,) is pivoted into the red join between present bulk mineralisation (M) and all remaining rocks of the intrusion (A) (Fig. 15). This demonstrates that the elemental ratios now preserved in the mineralisation are not primary and therefore cannot be used uncritically to model bulk compositions and processes.

Layering mechanism in Triple Group

The floor mineralisation is intimately related to the solidification and stratification of the Triple Group, and so an understanding of layering mechanisms that resulted in the formation of the Triple Group is a necessary constraint for a mineralisation model. The model for the layering mechanism is based on the stratigraphic distribution of liquid phases (P1 paragenesis) and mush

melt, as recorded by the distribution of interstitial phases that crystallised from interstitial mush melt (P2 paragenesis).

While only small amounts of plagioclase and clinopyroxene can be assigned to P2, e.g. in symplectites and fine-grained clinopyroxene mosaics (Fig. 6), much of the FeTi-oxides in the gabbros of the floor mineralization crystallised as part of the P2 paragenesis (Figs. 5 and 6). The stratigraphic variation in P1 ilmenite and P2 titanomagnetite is illustrated in Fig. 16. While Ilm_{24} forms small (~1mm) euhedral crystals dusted throughout the gabbros of the peaks, the stratigraphic variation of the ilmenite mode forms peaks that are, with only few exceptions, spaced 6-7m apart. The $TiMt_{24}/Ilm_{24}$ratio at these peaks is ~0.5, close to that expected for the liquidus paragenesis (Thy *et al.,* 2006). There is no systematic correlation between the modes of Ilm_{24} and $TiMt_{24}$ (Fig. 16), and all $TiMt_{24}$ (except for that contained in the Ilm_{24} peaks) is assigned to the P2 paragenesis of the mush melt. The observed $TiMt_{24}$/Ilm24 is in Fig. 17 compared to that expected from the experimental work of Thy *et al*. (2006). Most analysed samples have ratios >1, in contrast to the expected ratio of 0.5. The strong enrichment in Ti-magnetite of the host gabbros of the floor mineralisation suggests, as also illustrated in Fig. 6, the presence of abundant volumes of solids crystallised from interstitial mush melt. The implication of this is that *in situ* fractionation (*sensu* Langmuir, 1989) is likely to have played a significant role in the evolution of the gabbros.

The P1 paragenesis is, by volume, dominated by plagioclase and pyroxene, with disseminated small crystals of ilmenite and titanomagnetite (see section on host rock parageneses). All these minerals crystallised in the mush zone at the floor, but neither ilmenite nor titanomagnetite appear to play any role in the formation of modal layering and stratification of the P1 paragenesis. We suggest, therefore that the initial mineral stratification in the gabbros was predominantly a consequence of the gravitational separation between light plagioclase and dense pyroxene (with densities of 2.68 g cm^{-3} and 3.5 g cm^{-3}, respectively (Deer *et al.,* 1962)) in the mush melt of density 2.75 g cm^{-3} (calculated using the MELTS algorithm (Ghiorso & Sack

(1995)). Consequently, the primary stratification of the floor mush is defined by variations in the normative plagioclase/pyroxene ratio (plag/px).

Using the plag/px ratio, we suggest a new subdivision of the 65m of gabbro containing the floor mineralization, defining 4 macrolayers (Fig. 18). This new subdivision, based on the fundamental process of gravitationally-driven sorting of primocrysts, permits the development of a rigorous understanding of the mineralisation. We define melagabbros as those with plag/px < 0.7, and leucogabbro as those with plag/px >1. Mesogabbros are those with 0.7 < plag/px < 1.0. We label these four layers ML0, ML1, ML2 and ML2.1, where ML0 is the layer underlying L0, ML1 is that hosting L1, ML2 hosts L2, while ML2.1 is the macrolayer that overlies L2.

Three of the macrolayers, ML0, ML2 and ML2.1, are 13-14m thick and contain leucogabbro layers 5 m thick. In contrast, ML1 is ~20m thick and contains the 7.5m thick leucogabbro layer L1 with an additional, small, leucocratic section halfway up (e.g. plag/px of 0.85 at 1023m in drill core 90-22, shown in red in Appendix 4). This secondary leucogabbro layer at 1023m, together with the unusually thick L1, suggests the evolution of ML1 was unusual compared to the other three macrolayers.

The transition zones between macrolayers are composed of gabbros with normative plag/px in the range 1.0 - 1.8, and relatively low FeTi-oxide modes (<15 wt. % normative Mt+Ilm, shown in purple in Appendix 4). L0 below the Triple Group is not an L-layer *per se* but is actually one of these transition zones (Fig. 19). The "true" and petrographic L0 ($L0_p$, defined using our criterion of a high plag/px ratio) is ~5m thick and is located below the usual position attributed to L0 (which we will distinguish from our L0 by calling it $L0_{d+f}$) based on field identification and specific gravity (Andersen *et al.,* 1998). The high plag/px ratio of $L0_p$ is masked in the specific gravity data by an unusually large mode of $TiMt_{24}$ (associated with the P2 paragenesis).

The weakly defined leucogabbro layer halfway up ML1 is similar to $L0_p$ (identified in Appendix 4), which supports our hypothesis that the ML1 is actually a combination of two distinct

macrolayers. With this in mind, we suggest that, with the exception of ML1, the macrolayers in Triple Group have an average stratigraphic thickness of 13-14m.

We suggest that, following crystallisation in the mush zone, pyroxene and plagioclase were sorted by gravity to create a compositionally stratified mushy layer in which the crystal load increases from 0 % at its inner boundary to 100% at its outer, fully solidified, boundary. As the crystallization front in the floor moves toward the hot center during progressive solidification, increasing proportions of sinking pyroxene and floating plagioclase within the mushy layer interact. Following Bons *et al*. (2015), they form accumulations and barriers in the mush (Nielsen & Bernstein, 2009) with pyroxene on top and plagioclase below. $L0_{d+f}$, with a modal composition approximately that of the instantaneous modes (i.e. those of the contemporary liquidus paragenesis) of Thy *et al.* (2006), is an example of such a layer. These gravity-controlled transition layers subdivide the mush into conformable compartments in which plagioclase and melt accumulate in the upper parts while pyroxene and minor oxides accumulate at the floor. This is the process referred to by Nielsen & Bernstein (2009) as "self-stratification".

Conformable compartments separated by such transition layers act as self-contained magma chambers and are the starting point for the formation of the Skaergaard macrolayers: they can be thought of as "proto-macrolayers". These "proto-macrolayers" form the environment in which *in situ* fractionation occurs (*sensu* Langmuir, 1989), resulting in the crystallisation of plagioclase out of equilibrium with bulk liquid (Namur *et al*., 2014), the *in situ* formation of reactive Fe-rich silicate melts (Holness *et al*., 2011), the formation of pools of Fe-rich melt (Fig. 6), and the dissolution of droplets of sulphide melt (syn-magmatic digestion, Godel *et al*. (2014).

Timing of processes at floor, roof and walls

The last fundamental constraint required to model the mineralisation is a detailed correlation between melt evolution (expressed as *F*, the fraction of remaining melt) and the composition of liquidus plagioclase. The correlation between *F* values and plagioclase An% at specific points in the solidification history of the intrusion is summarised in Table 4, together with

calculations of the amount of crystallisation needed to reach sulphide saturation and silicate-silicate immiscibility. The data in Table 4 is a combination of *F* values provided in Table 2 and Appendix 6, and the compositions of plagioclase in compiled in Appendix 8.

The Cu anomaly in upper MZ, and at equivalent points in the roof and wall cumulates, is generally taken to signify the approximate timing of sulphide saturation in the bulk liquid (e.g. Andersen *et al.,* 1998; Salmonsen & Tegner, 2013; Nielsen, 2013). The Cu anomalies are, however, not exactly contemporaneous in the roof, walls and floor (Fig. 8). Furthermore, the Cu anomaly is diachronous across the floor (Fig. 2). This suggests that the precise timing of sulphide saturation is controlled by the local crystallisation environment.

In addition, the LLD for Pd, Pt and Au suggests the Pd/Pt of the bulk liquid was ~6 as the floor mineralization formed (at $F \sim 0.26$, Fig. 15a), whereas the precious metals supplied to the floor at this time have a Pd/Pt of 9 (shown by the orange dot in Figs. 15b, c). Because the Pd/Pt ratio of the precious metals supplied to the floor must record that of the silicate liquid in which the sulphide droplets equilibrated (see below), the ratio ~ 9 means that this silicate liquid must have been much more evolved than the contemporaneous bulk liquid.

The required amount of crystallisation of the silicate melt in which the sulphide droplets to increase Pd/Pt from 6 to 9 can be modelled assuming a maximum concentration of 10ppb Pt (a plausible maximum solubility in basaltic melt, see section on LLD) at the time the mineralisation formed (at $F \sim 0.26$). At a fixed concentration of 10ppb Pt, a Pd/Pt of 6 leads to a Pd concentration in the bulk liquid of 60ppb . To achieve a Pd/Pt ratio of 9 in the same liquid requires an increase of Pd concentration to 90 ppb. This requires the crystallisation of 1/3 of the melt in the mush zone and therefore *in situ* fractionation to a local value of $F \sim 0.18$ (calculated as 2/3 of the starting value of *F* of 0.26 for the bulk magma). We therefore suggest that the higher Pd/Pt ratio of the precious metals supplied to the floor mush is the result of *in situ* fractionation of bulk melt to local values of F=0.18 in the mush under the roof (corresponding to a liquid in equilibrium with plagioclase of An_{46-44} (Table 4), the same composition as that found in the floor mineralisation).

We conclude from this that the precious metal anomalies in neither the roof, walls nor floor were caused by sulphide saturation in contemporary bulk liquid with a composition corresponding to F=0.28 to 0.26.

The timing of the onset of silicate-silicate liquid immiscibility, and the formation of an emulsion rich in granophyric melt (Jakobsen *et al*., 2005; 2011; Veksler *et al*., 2009) is poorly constrained but has been suggested to have occurred between LZc to UZb times. Godel *et al*. (2014) argue that droplets of sulphide melt dissolve in Fe-rich mush melt and therefore that the formation of sulphide droplets (in either mush melt or bulk melt) must predate the onset of silicate-silicate liquid immiscibility. With sulphide saturation timed to $F \sim 0.18$ at the latest, the onset of silicate-silicate immiscibility and emulsion formation cannot have occurred until late UZa ($F < 0.15$) or even until the UZb boundary ($F \sim 0.1$), as originally suggested by Jakobsen *et al.* (2005). Significant quantities of melanogranophyre, believed to have crystallised from an immiscible Si-rich melt (McBirney & Nakamura, 1974), are found in UZb and c, but not in UZa, and we therefore suggest that silicate liquids only reach the two-liquid field when they attain compositions similar to that of bulk liquid at the UZa/b boundary ($F \sim 0.1$) (Table 4).

The low-PGE-zone is characterised by $F = 0.28$ - 0.26 and plagioclase An_{48} (Table 4). This zone partially overlaps with the timing of sulphide saturation in the roof mush (Fig. 14) (Table 4). The supply of precious metals to the floor mush was initiated while the low-PGE-zone formed and highlights the complexity of the mineralisation process(es). The timing of the effective removal of precious metals from the bulk liquid, and of the processes responsible for the mineralisation, must therefore have been confined to a window of crystallisation dating from the first signs of sulphide saturation in bulk liquid (as seen in roof and wall rocks at $F \sim 0.27$, Table 4) and ending at the uppermost Pd level in the floor mineralisation ($F \sim 0.25$, Table 4). The region of stratigraphy corresponding to this crystallisation window lies between the base of the low-PGE-zone (equivalent to Pd anomalies in roof and walls) and the lower part of the ML2.1 macrolayer (hosting Pd1).

MODELLING THE FLOOR MINERALISATION

In previous sections we developed and reviewed models for the structure of Triple Group and the mineralisation, the evolution of the bulk magma, processes involved in forming the layering, the relationship between parageneses of the host rocks and the mineralisation, and the timing of crystallisation and mineralisation processes relative to the evolution of the silicate melt. All of these place essential constraints on the mineralisation and crystallisation model we propose.

Mineralisation process in LPGEM (Pd6-Pd4)

Correlation between Pd+Pt and Pd/Pt

The association of an increase in Pd/Pt in LPGEM and the Pd-rich nature of the Pd5 mineralisation level (Fig. 13a) appears contradictory. The sulphide droplets and the grains of precious metal phases in LPGEM are very small (<1 to 100 μm, 15-20 μm average for precious metal grains (see Rudashevsky *et al*., (2014; 2015) together with statistics presented in mineralogical reports in Appendix 12)). The solubility of Pd in Cu-sulphide melt is of the order 10 wt% (Karup-Møller & Makovicky, 1999). A bulk rock concentration of ~150 ppm Cu (average for Pd5) and a maximum concentration of 5 ppm Pd+Pt in individual samples (Appendix 4) shows that the sulphide melt droplets were far from saturated in PGE in the Skaergaard mineralisation. Based on known *D*-values, sulphide droplets that were trapped in coexisting liquidus phases such as P1 ilmenite (Godel *et al*., 2014) would preserve a high Pd/Pt, whereas those droplets that experienced prolonged contact with mush liquid would have scavenged all Pd+Pt from their surroundings and would preserve the Pd/Pt of coexisting mush liquid modelled in Fig. 15a. The values of bulk liquid Pd/Pt that can be calculated from a given sample thus depend on the proportions of protected and equilibrated sulphide droplets. At Pd6 times, the bulk liquid Pd/Pt was 5 - 6 (Fig. 15a), the same as that of the bulk rocks at the base of Pd6 (Fig. 13a). In Pd6 sulphide melt was fully equilibrated with its silicate host and therefore the Pd/Pt of the sulphide droplets is the same as that of the melt from which they formed.

Based on peak Pd/Pt ratios of up to 35 at the time of supposed sulphide saturation in the roof (Table 2), a contemporary Pd/Pt in mush melt of 9 (Figs. 15b and c), and the empirical values recorded for Norilsk magmatism (Lightfoot & Keays, 2005), the increase in Pd/Pt as Pd and Pt partition into sulphide melt is of the order 4 - 5. With a Pd/Pt of the mush liquid constrained to be 5 - 6 at Pd6, an early-formed and fully protected sulphide droplet is expected to have a Pd/Pt of 20 – 30 in Pd6, of ~45 in Pd5, and of ~60 in Pd4**.** However**,** the Pd/Pt ratio is only close to the expected value in Pd4b (located in M0, the pyroxene-rich base of ML1). The high Pd/Pt in Pd4b is likely to be due to accumulation of sulphide droplets that were subsequently protected from re-equilibration in the base of the macrolayer. In Pd5, Pd/Pt reaches 25 and can be modelled as the average of 700ppb Pd+Pt at a Pd/Pt of 9 (composition CC, Fig. 15) and 2800ppb Pd+Pt at a Pd/Pt of 45 (in sulphide droplets protected in ilmenite and Ti-magnetite) resulting in an averaged peak concentration of 3500ppb at a Pd/Pt of 24.

Similar calculations can be made for all of the floor mineralisation, but the results of this approach remain hypothetical due to insufficient constraints on both the extent of subsequent re-equilibration and the primary compositions of sulphide droplets. Irrespective of this uncertainty, and as shown by the modelled LLD for Pd, Pt and Au (Fig. 15), Pd/Pt increased in the mush melt from which LPGEM formed, despite the preferred accumulation of Pd in the Pd5 mineralisation level. We argue that this is caused by a continued supply of PGE with high Pd/Pt from bulk liquid during the formation of LPGEM.

Mineralisation processes in the centre

While crystallisation from a common bulk liquid occurred simultaneously at the roof, walls and floor (Salmonsen & Tegner, 2013), there are distinct differences in the development of the three mush zones. The development of a detailed understanding of mush zone processes in roof, walls and floor of the intrusion requires a high geochemical resolution, but at present a sufficiently high resolution is only available for the floor, as provided by drill core 90-22 (Appendix 4). Given

these limitations, we propose a model based on the assumption of enrichment of the floor mush in precious metals by the accumulation of mush melt with high concentrations of dissolved precious metals, with Pd/Pt equilibrated to that of the coexisting silicate melt (e.g. Nielsen & Bernstein, 2009; Holwell & Keays, 2014).. We will develop a model for the transport of precious metals from the bulk liquid to the floor mush in a later section.

Pd6 shows a steady increase in Pd/Pt from 5 to 10 and a stepwise increase in Pd+Pt (Fig. 21). We see no correlation between Pd/Pt and Pd+Pt concentration (Fig. 21), no correlation between Pd+Pt and Cu (Fig. 21), but a correlation between Pd+Pt steps and high, or increasing, $TiMt_{24}$ (Fig. 21). PGE are disseminated through the gabbros and show intrusion-wide and strictly correlated distributions (see Fig. 7 in Andersen *et al.* (1998), and Appendix 3). Non-systematic geochemical variations are therefore unlikely to explain the stepped concentrations. The absence of correlation with Cu (Fig. 21) can be attributed to reaction between already formed droplets of sulphide melt and evolving mush melt (Godel *et al*., 2014). The correlation with $TiMt_{24}$ (P2 paragenesis, which can be taken as a proxy for Fe-rich mush melt) suggests the decrease of Pd+Pt was closely related to the distribution of, and reaction with, Fe-rich silicate melt in the floor mush.

In Pd5, the petrographic relations and grain morphologies shown in Figure 7 are consistent with the dissolution of droplets of sulphide melt, as suggested by Godel *et al.* (2014). At the level of the floor mineralisation the silicate mush melt will reach the two-liquid field at compositions locally equivalent to $F = 0.1$ (achieved after the crystallisation of 2/3 of the mass of melt that entered the mush zone, Table 4). Once the mush melt forms an emulsion, the immiscible silica-rich conjugate is likely to have been lost from the mush (Veksler *et al.,* 2009; Holness *et al*., 2011), consistent with the abundant melanogranophyre sills in the upper parts of the Skaergaard Layered Series stratigraphy (McBirney & Nakamura, 1974; Nielsen, 2004a). The remaining mush melt is therefore enriched in the Fe-rich immiscible conjugate, causing an increase in the solubility of S and the consequent dissolution of unprotected droplets of sulphide melt (Godel *et al*., 2014).

Such a process accounts for the absence of any correlation between Cu and precious metal concentrations in the mineralisation (Fig. 21).

Pd and Pt are concentrated in the remains of Cu-rich melt droplets, in Pd+Pt minerals, and in precious metal droplets dominated by skaergaardite (Fig. 7) that formed as a consequence of the dissolution of the Cu-sulphide component of the sulphide melt, in accordance with the experimental relations in the Cu-Pd-S system (Karup-Møller & Makovicky, 1999). The dissolution process is controlled by *D*-values: elements with lower *D*-values (e.g. Pb, Zn, Sb, Au,) dissolve preferentially and are made available for compaction-driven upwards redistribution of migrating mush melt. This process, that we suggest resulted in the formation of UPGEM (Fig. 13) may be analogous to the loss of S, As, Pd, Sb and Sn during re-melting and metamorphism of sulphide deposits (Frost *et al.*, 2002; Tomkins, 2007; Tomkins *et al.*, 2006; 2007).

We can summarise and combine the constraints placed on the processes forming the layering, the lithological and compositional correlations, and the timing of crystallisation and mineralization to create a model for the formation of LPGEM (Fig. 22):

1. Crystallisation of liquidus paragenesis P1 in the mush zone, followed by density stratification and the establishment of "proto-macrolayers" (section on layering in Triple Group, Fig. 18).
2. *In situ* fractionation and sulphide saturation after ~27% crystallisation (at local F=0.18, Table 4) of the silicate liquid in the "proto-macrolayers".
3. Sulphide droplets form and scavenge precious metals from the surrounding silicate melt. The droplets trapped in either basal accumulations, such as Pd4b (Fig. 13), or in liquidus phases, preserve high Pd/Pt, whereas droplets disseminated in the mush melt re-equilibrate to lower Pd/Pt (see section on controls on Pd/Pt in LPGEM).
4. The mush liquid hits the two-liquid field after crystallisation of ~60% of the melt volume (at local F = 0.1, Table 4), followed by the loss of an emulsion rich in the Si-rich conjugate. The solubility of S increases in the remaining highly Fe-rich mush melt.

Droplets of molten sulphide melt re-equilibrate and are partly or fully dissolved, leaving behind precious metal minerals and PGE-enriched droplets disseminated throughout the gabbros (see Fig. 7).

5. Mush silicate melt with its load of incompatible elements and dissolved precious metal is driven upwards by compaction to form overlying mineralization levels.

Mineralisation processes near the margin of the intrusion

Near the margins of the intrusion, gold is located in the Pd4 level of LPGEM (as recorded in drill cores 90-23A (Fig. 2) and 90-14 (Appendix 3)) (Andersen *et al.,* 1998; Nielsen, 2005). In drill core 90-23A, LPGEM is a fully fractionated mineralization, compared to its entirely skaergaardite-dominated and relatively simple paragenesis in central drill cores, e.g. 90-24 (Nielsen *et al.,* 2005) in which it is strongly depleted in elements such as Pb, Sn, As, S and Au. The differences in paragenesis are confirmed by comparison of the average precious metal ratios of the entire mineralisation in (central) drill core 90-22 (Pd6 to UAuM, ~43m, with a Pd/Pt of ~13, and a Au/Pd of ~0.25) and the Pd6-Pd4 interval in (marginal) drill core 90-23A (~19m thick, with Pd/Pt of ~12.7 and a Au/Pd of ~0.2).

While the 19m thick mineralized interval from Pd6 to Pd4 in drill core 90-23A could be mistaken for a condensed version of the 43m thick mineralisation (Pd6-UAuM) in central parts of the intrusion, the preservation of the stratigraphic thickness of the lithological succession across the floor of the intrusion (Appendix 1) shows that this cannot be the case. We conclude that the drill cores from the margin of the intrusion do, in fact, contain a fully evolved mineralization in LPGEM, with Au 5-10m above Pd5. Because *D*-values fall in the order Pd>Pt>Au>Cu, this demonstrates the cessation of precious metal supply to the floor mush at Pd4 times.

The MZ gabbros near the margins of the intrusion contain paired pockets of crystallised Fe-rich and Si-rich liquids whereas stratigraphically equivalent gabbros in the centre of the intrusion are characterized by reactive symplectites (Holness *et al.,* 2011). The reactive symplectites are the record of the loss of a conjugate Si-rich melt, whereas the paired late-stage

pockets indicate no separation of conjugate melts (Holness *et al*., 2011), suggestive of greater retention of mush melt at the margins of the intrusion floor. This conclusion is consistent with the precious metal parageneses and the common occurrence of primary hydrous silicates in the marginal drill core 90-23A, which also point to greater retention of (evolved, volatile-rich) mush melt and incompatible elements including dissolved precious metals. This greater retention of the mush melt at the intrusion margins, and the associated retention of precious metals in LPGEM after their primary deposition, is most probably due to the relatively fast cooling and a lower mush permeability near the walls of the intrusion.

Mineralisation processes in UPGEM (Pd3-Pd1)

In central cores, the mineralization is distributed up into ML2.1 (Fig. 18), despite the termination of precious metal supply from bulk liquid at Pd4 and ML1 times. Precious metals in central cores that contain one or more mineralisation level (i.e. any mineralisation levels stratigraphically higher than Pd4) must therefore have been affected by the protracted upwards redistribution and fractionation of precious metals already accumulated in LPGEM. We therefore refer to Pd3, Pd2 and Pd1 as secondary mineralisation levels. Similar petrographic relationships in gabbros of UPGEM and LPGEM of central drill cores (e.g. Nielsen *et al.*, 2003a-e; Rudashevsky *et al.*, 2009a-b; 2012a-i; Appendix 12) show that the same suite of processes that we outlined for LPGEM must have occurred in all Pd levels.

Although the proportions of PGE-rich arsenides and sulphides increase upwards (Nielsen *et al.*, 2005), these minerals are only a very minor component of the platinum group mineral (PGM) paragenesis, which is strongly dominated by skaergaardite and (Pd,Pt,Au,Cu) alloys (see Cabri (2004), Rudashevsky *et al.* (2014; 2015), Godel *et al.* (2014) and, in Appendix 12, Nielsen *et al.* (2003a-e; 2005), Rudashevsky & Rudashevsky (2005a-b; 2006a-b), and Rudashevsky *et al.* (2004; 2009a-b; 2010a-d; 2012a-i; 2013a-b)). The Pb, Sb and Sn substitution in PGMs common in LPGEM at the margins of the intrusion is very limited in UPGEM in the centre of the

mineralisation, where we infer that these elements were lost from the mush both from LPGEM (Pd6, Pd5 and Pd4) and from UPGEM (Pd3, Pd2 and Pd1).

All Pd levels in UPGEM, the secondary Pd levels, have very high Pd/Pt at their base (Fig. 13a), and each Pd level shows fractionation from high to low Pd/Pt with increasing height (Figs. 13a, b). These observations can be explained if we envisage each Pd level as a fractionation compartment, i.e. a small semi-closed magma chamber rich in mush melt. The very high Pd/Pt ratios at the base of the secondary reefs are interpreted as the result of trapping high Pd/Pt sulphide droplets that formed early, when the mush melt in the "proto-macrolayers" was first saturated in sulphide (in an analogous manner to that proposed above for the Pd4b level). The suggested presence of inclusions with high Pd/Pt provides evidence for the *in situ* crystallisation of their host phases. Further fractionation of the mush melt, together with upwards migration during progressive solidification, provides an explanation for the systematic depletion of Pd upwards through the stratigraphy and the general decrease in Pd/Pt in UPGEM (Fig. 13b).

The overall pattern of stratigraphic variations of PGE concentrations in UPGEM is mimicked by those of $TiMt_{24}$, The corresponding $TiMt_{24}$ anomaly is below the PGE peaks in Pd3, close to the peaks in Pd2, and coincides with the peak in Pd1 (Fig. 23). This systematic reduction of stratigraphic separation between correlated PGE and $TiMt_{24}$ peaks in UPGEM suggests a systematic change of the relative timing of sulphide saturation (initially equivalent to $F \sim 0.18$) and the crystallisation of $TiMt_{24}$ (equivalent to $F \sim 0.1$) from Fe-rich silicate melt in the evolving mush melt of the "proto-macrolayers". This change may reflect a continued increase in Fe content of the mush melt and a consequently increasing delay in sulphide saturation, which initially occurred at an equivalent $F \sim 0.18$ but occurred only at $F \sim 0.1$ in the more Fe-rich mush melt formed during *in situ* fractionation. Testing this hypothesis is not yet possible both because of the extensive recrystallisation of the FeTi-oxides, and because we don't know how much $TiMt_{24}$ crystallised from the bulk liquid and how much crystallised from mush melt both prior to, and after, loss of the Si-rich conjugate from the mush.

The final stage of our model for the evolution for each "proto-macrolayer" is the compaction-driven upwards loss of residual Fe-rich mush melt into the overlying "proto-macrolayer", bringing any dissolved metals and other incompatible elements with it. In most of the central cores, the Au-rich upper part of the mineralisation divides in two (e.g. Fig. 2a, see also Watts, Griffis & McOuat Ltd. (1991) and Hanghoj (2005)). The lower Au peak is hosted in UPGEM in the uppermost Pd level in any given core, irrespective of the actual number of Pd levels present. The peak commonly contains ~1 ppm Au, which forms tetra-auricupride (AuCu) and intermetallic alloys of PGE, Au and Cu (e.g. Rudashevsky & Rudashevsky, 2005a; Rudashevsky *et al.*, 2010b; Appendix 12), as well as substituting in skaergaardite (PdCu, Andersen *et al.*, 1998; Nielsen *et al.*, 2005). The upper Au-rich, but PGE-poor level (the Upper Au Mineralisation level, UAuM), is distinct in mineralogy, petrography and petrographic relations, and is discussed in the following section.

This model for the formation of UPGEM is based on the concept of an interconnected system of mushy zones in a stacked and upward migrating succession of "proto-macrolayers", each subjected to addition, fractionation, and removal of mush melt. The scenario we describe for the formation of the secondary mineralisation levels of UPGEM has similarities with the "Palladium" model of Boudreau (2004) who stated "…the presence of PGE alloys and other insoluble PGE-rich phases can easily form as the result of loss of S to migrating sulphide-undersaturated fluid or silicate liquid; these phases can precipitate once the sulphide host has been resorbed. For the fluid-free models, the Pd zones may be ephemeral, as Pd metal will readily re-dissolve into sulphide once the interstitial liquid reaches sulphide saturation".

Mineralisation processes in UAuM

UAuM levels are always located in, or above, the uppermost level of PGE concentration (irrespective of stratigraphic position), but are below, or coincide with, the first major Cu mineralisation level (Fig. 2). Au minerals and PGE-bearing phases occur together with hydrous silicates at the grain boundaries (Rudashevsky *et al.*, 2014). The mineralogy of UAuM is

characterised by 92 vol. % tetra-auricuride (AuCu) and no recorded skaergaardite (PdCu), distinctly different to the 27% and 61 vol. %, respectively, of these two minerals in Pd1 (Table 5). Following Rudashevsky *et al*. (2014) we interpret UAuM as a late mineralisation event formed in already crystallised gabbro and caused by the migration of the volatile-bearing residual of the Fe-rich immiscible silicate melt enriched in Au. The loss of Au from the LPGEM and UPGEM is modelled by the pivoting of elemental balances in bulk liquid modelling (Figs. 15b, c), and trapping at redox barriers (Godel *et al.*, 2014). That the residual mush melts may have coexisted with a free volatile phase is supported by the occurrence of Cl-apatite in upper MZ (Sonnenthal, 1992) and by the presence of round, amphibole-dominated crystallised inclusions of silicate melt in ilmenite crystals of the mineralisation (Godel *et al.,* 2014). A droplet of silicate melt trapped together with a bubble of a free volatile phase, will crystallise a mineral assemblage dominated by hydrous silicate phases.

Formation of Cu reefs (CuM)

No clear correlation links the stratigraphic height or composition of Pd levels, UAuM and the stratigraphically lowest major accumulation of Cu. In drill core 90-22 (from the center of the intrusion floor) the first major Cu peak occurs 43m above Pd5 and ~3m above UAuM, whereas in marginal core 90-23A, the Cu peak is only ~20m above Pd5, but 10m above UAuM (Fig. 2). Cu anomalies in the floor do not record a "global" contemporaneous event in the intrusion. At the present sample resolution, seven Cu-rich levels, with an average spacing of 13-14m, are observed over ~100m of stratigraphy in upper MZ and into the base of UZa (Fig. 24). The spacing is equivalent to the height of macrolayers in the Triple Group (Fig. 18) and suggests that, just as in the Pd levels, sulphide saturation and the accumulation of Cu were caused by local sulphide saturation in melt of the floor mush in the stratigraphic section between F=0.25 and 0.20 and prior to bulk liquid sulphide saturation at $F \sim 0.18$ (Table 4).

PRECIOUS METAL DEPLETION OF BULK MAGMA

The precious metal depletion of the bulk magma, resulting in the deposition of precious metals in the floor mush, can be thought of as the downers stage of the mineralisation process. The timing of this stage, and the mechanism by which it occurred, can be constrained by a consideration of likely mass movements within the chamber as a whole.

Convection in the bulk magma ensured that the liquidus (P1) paragenesis was the same at floor, roof and walls (e.g. Salmonsen & Tegner, 2013). However, the composition and evolution of the interstitial melt in the mush differed significantly from that of the contemporaneous bulk liquid. Gravitational sorting in the floor mush created "proto-macrolayers" by selective floatation and sinking of crystalline phases, while the onset of liquid immiscibility in the mush resulted in the progressive loss of the buoyant Si-rich conjugate. The P2 paragenesis crystallised from resultant Fe-rich mush melt (Fig. 22). The spatial distribution of reactive symplectites suggested that the recycling of Si-rich melts from the mush to the bulk magma occurred from LZb to UZa times (Holness *et al*., 2011; Humphreys *et al.,* 2011).

The occurrence of paired Si-rich and Fe-rich melt inclusions (signifying crystallisation from an emulsion) and the absence of reactive melt inclusions in roof gabbros (Holness *et al*., 2011) demonstrate that the scenario in the roof mush was complementary to that in the floor. During *in situ* fractionation, mush melt accumulated in the roof zone would have reached silicate-silicate liquid immiscibility at local $F = 0.1$. Emulsion rich in granophyre (Veksler *et al.,* 2009) would have been buoyant and remained in the roof mush, whereas a conjugate, dense, Fe-rich melt would sink, be entrained in the convecting bulk magma and be carried to the floor. The addition of this roof-derived Fe-rich liquid would have increased the Fe concentration in the floor mush, possibly contributing to the delay in local sulphide saturation (Table 4).

Additional support for this inferred behaviour of the mush melt at the roof is provided by the observed replacement of magnetite in roof gabbro by Fe-rich olivine and pyroxene in a reaction with granophyric melt (QFM buffer, Fig. 25b). In a complementary manner, the fingerprint of extensive *in situ* fractionation and loss of residual melt from Lower Zone gabbros is

apparent in the occurrence of apatite crystals along grain boundaries (Fig. 25a). Apatite would first crystallise in melt of the LZ mush equivalent to UZb ($F \sim 0.1$).

Because the bulk liquid was well mixed, it is expected that sulphide would first saturate in the roof mush melt at $F \sim 0.18$, in an analogous manner to the floor mush melt (Table 4). Sulphide droplets would form in the roof mush, and, by analogy with the model developed for the floor mush, remain disseminated in the mush and equilibrate chemically with the mush melt, resulting in equilibrium Pd/Pt and Au/Pd ratios. Higher in the roof mush, where temperatures were lower, immiscible Fe-rich melts would form once the composition of the mush melt attained that equivalent to UZa/b ($F \sim 0.1$). Fe-rich mush melt would sink relative to granophyre-rich emulsion, dissolving any droplets of sulphide melt it encountered, and sink into the convecting bulk liquid (Fig. 26). At upper MZ times, assuming a load of liquidus and adcumulus crystals (P1 paragenesis) of 30%, sulphide saturation would be reached when 35-40 % mush melt remained, while the silicate-silicate immiscibility field would be reached when 25-30% mush melt remained.

Pd, Pt, and Au, initially partitioned into droplets of sulphide melt equilibrated to the Pd/Pt and Au/Pd of melt in the roof mush (CC of Fig. 15), would end up in the floor mush and be available for the mineralization processes described in previous sections (LPGEM). The concentration of precious metals and entrapment in droplets of sulphide melt occurred in the mush zones between hot bulk liquid and solidified gabbro and in equilibrium with melt whose composition was evolved relative to the contemporaneous bulk melt.

DISCUSSION

Concordant or transgressive mineralisation levels?

Our detailed survey (Appendices 1-3 and 5) documents the unequivocally fully concordant relationship between the mineralised levels and the modal layering. The main features include the compositional zoning within the individual levels as well as the vertical changes between successive levels. This structure, which was first documented by Andersen *et al.* (1998) and Nielsen *et al.* (2005), is supported by a wealth of new mineralogical and geochemical data (reports

in Appendix 12). It is of some concern to us, therefore, that Holwell & Keays (2014) appear to discount the observations that led to this interpretation of the structure in favour of a structure comprising a lower, concordant, PGE-zone, with upper Au and Cu zones that are transgressive to the modal layering. Their model of the Skaergaard mineralisation fails to explain the intricate structure and correlations between mineralisation levels across the intrusion, the detailed evolution of the individual levels, and the larger-scale stratigraphic correlations. They ignore the connections between the mineralisation and the primary igneous stratigraphy, and provide no petrological observations to substantiate their claims.

An illustration of the consequences of ignoring these connections is provided by the lower stratigraphic position of the Au level at the intrusion margin (in Pd4 in ML1) compared to the centre (where the Au level occurs in Pd1 in ML2.1). Unless the layers grew outwards from the centre (a suggestion we find entirely untenable) the Au level at the intrusion margins must have formed well before the gabbros that host the Au level at the centre of the intrusion, in contradiction to its formation as a high-temperature, syn-magmatic mineralisation as suggested by Holwell & Keays (2014). The structural model of Holwell & Keays (2014) is incompatible with the basic observations of the structure of the mineralisation and conflicts with their own conclusions.

Scavenging of precious metals from the bulk magma

Our suggested mechanism of accumulation of precious metals in sulphides at the roof is related to sulphide saturation within melt evolved in the mush zone itself. The effective extraction of precious metals by their sequestration in droplets of sulphide melt between F= 0.28 and 0.26 (Table 4), might suggest that the sulphide droplets were in chemical contact with a large volume of melt (large R-factor, Campbell & Naldrett, 1979). This is usually supposed to be achieved as the droplets sink through the entire height of the magma chamber. However, it is difficult to see how a droplet of Cu-sulphide melt, only ~100μm in diameter, could survive such a journey, or how such scavenging could be achieved if the droplets are transported in down-going plumes of

melt, since they would equilibrate only with the volume of melt in which they were transported.

The alternative we propose for the Skaergaard intrusion is that the precious metals are continuously processed in mush zones due to extensive *in situ* fractionation of mush melt. The sulphide melt droplets do not sink, but are re-dissolved (at local $F = 0.1$) in subsequently formed immiscible Fe-rich mush melt, and it is this Fe-rich melt that concentrates and transports the precious metals to the floor. It is precisely this kind of melt that Nielsen & Bernstein (2009), Nielsen (2013), Holwell & Keays (2014), and Holwell *et al.* (2014) call on for the accumulation of precious metals in the floor mush of the intrusion. This model is radically different from that requiring interaction between large volumes of silicate melt and sulphide droplets during their descent in magma chambers (e.g. Naldrett, 2004).

Comparison to other mineralisation models

The formation of reef-type PGE mineralisations has received significant scientific attention due to their importance as mineral resources, vastly dominated by occurrences in the Bushveld complex (e.g. Cawthorn, 1999). The two main types of models the "downers" and "uppers" have, in a multitude of variants, been applied to known reef-type deposits (reviewed by Naldrett (2004; 2011)). Our newly proposed model of the Skaergaard mineralisation, based on detailed study of the petrographic and geochemical correlations, is dominated by the effects of *in situ* fractionation within mush zones. The only exception is the observed variation of Pd/Pt, which we attribute to fractionation in the bulk liquid.

Mineralisation processes based on the transport of precious metals by migrating mush melts were proposed by Boudreau (2004), whose model produces repeated deposition, reaction and dissolution of sulphide melt droplets in migrating mush melt in a similar manner to the model we suggest for UPGEM. In a very detailed geochemical study of the Merensky Reef, Wilson & Chunnett (2006) find a "direct genetic link between the mineralisation and the rock-forming processes". They find that the sulphides and PGMs are not evenly distributed in the host rocks but,

just as in Skaergaard, relate to specific types of parageneses and melts in the matrix of the cumulate rocks.

Most other models proposed for the genesis of the Skaergaard mineralisation have assumed deposition of sulphide from bulk liquid. Andersen (2006) suggests a primary sulphide paragenesis of pyrrhotite and chalcopyrite (Cu-bearing Fe-rich sulphide melt), whereas other models do not constrain the composition of the sulphide melt supplied to the floor. In Skaergaard, all sulphide droplets and clots investigated to date in both roof and floor are Cu-rich with a bulk composition near that of bornite (see section on petrography of sulphides). Magnetite is observed in a few "bornite" droplets, but remains an exception. Cu-sulphides, with the shape of negative crystals within ilmenite (Godel *et al.,* 2014) must have originally been droplets of Cu-rich sulphide melt that were trapped in their host at magmatic temperatures (e.g. Godel *et al*., 2014). Petrographic evidence in support of the Cu-bearing but Fe-rich sulphide melt proposed in Andersen (2006) is yet to be provided.

Nielsen & Bernstein (2009), as well as Holwell & Keays (2014), relate the floor mineralisation to the presence of Fe-rich mush melt. Holwell & Keays (2014) explain the repetition of the Pd levels by suggesting that this mush melt remained perched at the sulphide saturation level for a protracted time, but offer no evidence to support this hypothesis. In contrast, we model the repetition of mineralisation levels within the context of the layering process in the gabbros by considering the solubility of sulphide as affected by *in situ* fractionation and immiscibility between Fe- and Si-rich silicate melts..

Consequences for solidification of the Skaergaard intrusion

In its classic form the cumulus paradigm builds on the assumption that continuously homogenised bulk magma crystallises successive liquidus mineral assemblages that accumulate mainly on the magma chamber floor and, to a lesser extent, under the roof and on the walls (Wager & Brown, 1968). Implicit in this model is that the phases in the mush zones are in equilibrium with a bulk liquid of a given *F* value. However, it is clear from the abundant reactions

between the liquidus minerals and the mush liquid (Fig. 5) that the cumulus minerals were out of equilibrium with contemporary bulk melts (Holness *et al.,* 2011; Namur *et al*., 2014), pointing to extensive *in situ* fractionation in mush zones. Solidification actually involved the departure of some portion of the mush melt, leaving behind solids and melts with a range of compositions along the LLD. Tight control on the relative timing and evolution of melt in the mush zone is thus required for detailed modelling of fractionation and crystallisation processes of the bulk liquid in the intrusion and for the budget of incompatible elements (Langmuir, 1989).

The presence of reactive symplectites from LZb to UZa in the central part of the intrusion (Holness *et al*., 2011) and the common occurrence of Fe-rich melt inclusions in LZc (Jakobsen *et al.,* 2011) provide a record of the formation of Fe-rich immiscible melt in mush zones throughout most of the solidification of the floor cumulates and by analogy also in contemporaneous roof mush. Fe-rich melt would have sunk from the roof mush from upper LZ times. The amount of this Fe-rich melt would have been very small, but would have increased in importance as the bulk liquid evolved and approached the immiscibility field between Fe- and Si-rich melts (Jakobsen *et al*., 2005). Complementary UBS bulk rocks are quartz normative and contain cognate granophyre clots (Salmonsen *et al.,* 2014) indicating that granophyre-rich emulsions were retained in the roof mush. The complementary nature of liquid evolution in the roof and floor and our suggested redistribution of Fe in the intrusion (Fig. 26) provide possible explanations for the multitude of suggested LLDs for the Skaergaard intrusion (e.g. Fig. 1 in Jakobsen *et al.*, 2005). LLD models published prior to Salmonsen & Tegner (2013) and Salmonsen *et al*. (2014) should be revised to incorporate appropriate proportions of granophyre in roof gabbros (UBS). Models based on phase relation (e.g. Toplis & Carrol, 1996) and plausible parental bulk liquid compositions (e.g. Thy *et al.*, 2009), and models that estimate the proportion of granophyre on bulk chemical balances (e.g. Nielsen, 2004a) may need no revision. We note in passing that the very Fe-rich experimental melts of McBirney & Nakamura (1974) are interstitial melts produced by limited partial melting of floor

cumulates, and are not necessarily representative of melts on the LLD of the bulk liquid. They may, however, be eutectic melts of the P2 paragenesis.

Charlier & Grove (2012) showed that most basaltic liquids have the potential to form coexisting immiscible Si-rich and Fe-rich melts during their fractionation. Intrusion-scale re-distribution of Fe via the preferential movement of the conjugate components of immiscible silicate melts may therefore be common to mafic complexes. The sum of our observations is that the bulk liquid evolution in mafic intrusions cannot be based only on the floor cumulates. All parts of the intrusion must be included in the modelling of the parental bulk liquid, the magmatic evolution, as well as any mineralisation processes. The re-distribution of immiscible Fe- and Si-rich liquids between the floor and the roof means that ignoring the walls and roof will result in models that are unrepresentative of the evolution of the bulk liquid of the intrusion.

ACKNOWLEDGEMENTS

The present study represents many years of co-operation and data gathering by scientists of the Skaergaard Group, together with discussions and evaluation of a multitude of petrogenetic schemes for the evolution of the mineralisation and the Skaergaard intrusion in general. Peter Thy is thanked for access to EMP data for plagioclase in compositions of the Skaergaard Standard profile. The authors have been inspired by countless discussions and debates with colleagues on the crystallisation of gabbro intrusions and precious metal deposits in mafic intrusions. To name a few, we thank: C. Kent Brooks, Richard Wilson, Dan McKenzie, Alexander R. McBirney, Richard Naslund, Emil Makowicky, Neil Irvine, Steve Barnes, Lotte M. Larsen, Asger K. Pedersen, Belinda Godel, Peter Thy, Charles E. Lesher, Andrew Putnis, Michael Zienteck, Reid Keays, Olivier Namur, Rais Latypov, Lewellyn Pilbeam, Jochen Kolb, and Diego Rosa. Susanne Rømer is thanked for technical assistance with illustrations.

REFERENCES

Andersen, J. C. Ø. (1996). The Skaergaard intrusion and the Platinova gold and palladium deposit, Kangerlussuaq area, East Greenland: Ph.D.-thesis, Copenhagen University, 230 p.

Andersen, J.C.O. (2006). Postmagmatic sulfur loss in the Skaergaard Intrusion: Implications for the formation of the Platinova Reef. *Lithos* **92**, 198-221.

Andersen, J.C.Ø., Rasmussen, H., Nielsen, T.F.D. & Rønsbo, J.C. (1998). The Triple Group and the Platinova gold and palladium reefs in the Skaergaard Intrusion: stratigraphic and petrographic relations. *Economic Geology* **93**, 488-509.

Bernstein, S. & Nielsen, T.F.D. (2004). Chemical stratigraphy in the Skaergaard intrusion. *GEUS report* **2004/123**, 31 pp. + CD.

Bezmen, N.I., Gorbachev, P.N., Shalynin, A.I., Asif, M. & Naldrett, A.J. (2008). Solubility of platinum and palladium in silicate melts under high water pressure as a function of redox conditions. *Petrology* **16**,161-176.

Bird, D.K., Brooks, C.K.., Gannicott, R.A., & Turner, P.A., (1991), A gold-bearing horizon in the Skaergaard Intrusion, East Greenland. *Economic Geology* **86**, 1083-1092.

Bollingberg, K. (1995). Textural and chemical evolution of the FeTi-minerals during the late- and post-magmatic cooling of the Skaergaard intrusion, East Greenland. PhD thesis, University of Copenhagen, 112 pp plus appendices (pdf available on request).

Bons, P.D., Baur, A., Elburg, M.A., Lindhuber, M.J., Marks, M.A.W., Soesso, A., van Muligen, B.P., & Walte, N.P. (2015). Layered intrusions and traffic jams. *Geology* **43**, 71-74.

Boudeau, A. (2004). PALLADIUM, a program to model the chromatographic separation of the platinum-group elements, base metals and sulfur in a solidifying pile of igneous crystals. *The Canadian Mineralogist* **42**, 393-403

Boudreau, A.E. & McCallum, I.S. (1992) Concentration of Platinum-group elements by magmatic fluids in layered intrusions. *Economic Geology* **87**, 1830-1848.

Boudreau, A.E. & McBirney, A.R. (1997). The Skaergaard Layered Series. Part III. Non-dynamic Layering. *Journal of Petrology* **38**, 1003-1020.

Boudreau, A.E. & Meurer, W.P. (1999) Chromatographic separation of the platinum-group elements, gold, base metals and sulfur during degassing of a compacting and solidifying crystal pile. *Contributions to Mineralogy and Petrology* **134**, 174-185

Cabri, L. (2004). A mineralogical evaluation of two samples for Skaergaard Minerals Corp, License No. 2000/10. In: Skaergaard Minerals Corporation (2004): Report on exploration activities on Skaergaard Mineral license during 2003, Appendix 4, 65pp. appendices (in archive of the Geological Survey of Denmark and Greenland, GRF no. 21840; available on-line).

Campbell, H. & Naldrett, A.J. (1979). The influence of silicate:sulfide ratios on the geochemistry of magmatic. *Economic Geology* **74**, 1503-1506.

Cawthorm, R.G. 1999: The platinum and palladium resources of the Bushveld complex. South *African Journal of Science* **95**, 481-489. N

Charlier, B. & Grove, T.L. (2012). Experiments on liquid immiscibility along tholeiitic liquid lines of descent. *Contributions to Mineralogy and Petrology* **164**, 27-44.

Deer, W.A., Howie, R.A.& Zussman, J. (1962). *An Introduction to the Rock-forming Minerals*. London: Longmans, 528pp.

Eales, H. V. & Cawthorn, R. G. (1996). The Bushveld Complex. In: Cawthorn, R. G. (ed.) *Layered Intrusions*. Amsterdam: Elsevier, 181–229.

Ertel, W., Dingwell, D.B. & Sylvester, P.J. (2008). Siderophile elements in silicate melts: a review of the mechanically assisted equilibration technique and the nanonugget issue. *Chemical Geology* **248**, 119-139.

Farges, F., Neuville, D.R. & Brown, G.E. Jr (1999). Structural investigation of platinum in silicate glasses. *American Mineralogist* **84**,1562-1568.

Frost, B.R., Mavgrogenes, J.A. & Tompkins, A.G. (2002). Partial melting of sulphide ore deposits during medium- and high-grade metamorphism. *The Canadian Mineralogist* **40**, 1-18.

Ghiorso, M.S. & Sack, R.O. (1995). Chemical mass transfer in magmatic processes. IV. A revised and internally consistent thermodynamic model for the interpolation and the extrapolation of liquid-solid equilibria in magmatic systems at elevated temperatures and pressures. *Contributions to mineralogy and Petrology*, **119**, 197-212

Godel, B., Rudashevsky, N.S., Nielsen, T.F.D., Barnes, S.J., & Rudashevsky, V.N. (2014). Constraints on the origin of the Skaergaard intrusion Cu-Pd mineralisation: insights from high-resolution X-ray computed tomography. *Lithos* **190-191**, 27-36.

Hanghoj, K. (2005). Report on exploration activities in 2004 on Skaergaard license no. 2005/09. Internal report, Skaergaard Minerals., Corp, 51 pp, 1 appendix: gochemical analyses, core recovery, drill hole survey, 175 pp. (In archive of the Geological Survey of Denmark and Greenland, report GRF 21895; available on-line).

Holness, M.B., Tegner, C., Namur, O. & Pilbeam, L. (2015) The earliest history of the Skaergaard magma chamber: a textural and geochemical study of the Cambridge Drill Core. *Journal of Petrology*, in press.

Holness, M.B, Tegner, C., Nielsen, T.F.D., Stripp, G. & Morse, S.A. (2007). A textural record of solidification and cooling in the Skaergaard intrusion, East Greenland. *Journal of Petrology* **48**, 2359-2377.

Holness, M.B., Stripp, G., Humphreys, M.C.S., Veksler, I.V., Nielsen, T.F.D. & Tegner, C. (2011). Silicate liquid immiscibility within the crystal mush: late-stage magmatic microstructures in the Skaergaard intrusion, east Greenland. *Journal of Petrology* **52**, 175-222.

Holwell, D. & Keays, R.R. (2014). The formation of low-volume, high-tenor magmatic PGE-Au sulfide mineralisation in closed systems: evidence from precious and base metal geochemistry of the Platinova reef, Skaergaard Intrusion, East Greenland. *Economic Geology* **109**, 387-406.

Holwell, D.A., Keats, R.R., McDonald, I., Williams, M. R. (2014): Super-concentration of PGE, Au, Se, and Te by sulfide liquid dissolution in closed systems: Evidence from the Skaergaard intrusion, East Greenland. *Acta Geologica Sinica* (English edition) 88, suppl. 2, 283-284.

Hoover, J.D. (1989). The Chilled Marginal Gabbro and Other Contact Rocks of the Skaergaard Intrusion. *Journal of Petrology* **30**, 441-476.

Humphreys, M.S.C. (2011). Silicate liquid immiscibility within the crystal mush: evidence from Ti in plagioclase from the Skaergaard Intrusion. *Journal of Petrology* **52**, 147-174.

Irvine, T.N., Andersen, J.C.Ø., & Brooks, C.K. (1998). Included blocks (and blocks within blocks) in the Skaergaard Intrusion: geological relations and the origins of rhythmic modally graded layers. *Geological Society of America Bulletin* **110**, 1398-1447.

Jakobsen, J.K., Veksler, I.V., Tegner, C. & Brooks, C.K. (2005). Immiscible iron- and silica-rich melts in basalt petrogenesis documented in the Skaergaard intrusion. *Geology* **33**, 885-888.

Jakobsen, J.K., Veksler, I.V., Tegner, C. & Brooks, C.K. (2011). Crystallization of the Skaergaard intrusion from an emulsion of immiscible iron- and silica-rich liquids: Evidence from melt inclusions in plagioclase. *Journal of Petrology* **52**, 345-373.

Karup-Møller, S. & Makovicky, E. (1999). The phase system Cu–Pd–S at 900˚, 725˚, and 400˚C. *Neues Jahrbuch Mineral. Monatshefte* **1999**, 551-567.

Karup-Møller, S., Makovicky, E. & Barnes, S-J. (2008). The metal-rich portions of the phase system Cu-Fe-Pd-S at 1000°C, 900°C and 725°C. Implications for mineralisation in the Skaergaard intrusion. *Mineralogical Magazine* **72**, 947-951.

Keays, R. & Tegner, C. (2013). Controls on the magmatic PGE and Au mineralisations in the Skaergaard intrusion. *Abstract EGU General Assembly 2013, Geophysical Research Abstracts* **15**, ABS EUG2013-2655.

Kystol, J. & Larsen, L.M. (1999). Analytical procedures in the Rock Geochemical Laboratory of the Geological Survey of Denmark and Greenland. *Geology of Greenland Survey Bulletin* **184**, 59-62.

Langmuir, C. H. (1989). Geochemical consequences of in situ crystallization. *Nature* **340**, 199-205.

Lightfoot, P.C. & Keays, R R. (2005). Siderophile and chalcophile metal variations in flood basalts from the Siberian Trap, Noril'sk Region: Implications for the origin of the Ni-Cu-PGE sulfide ores. *Economic Geology,* **100**, 439-

McBirney, A. R. (1989). The Skaergaard Layered Series: 1. Structure and average compositions. *Journal of Petrology* **30**, 363-397.

McBirney, A.R. (1996).The Skaergaard Intrusion, in: Cawthorn, R.G. (ed.) *Layered Intrusions*. Amsterdam: Elsevier, 147-180.

McBirney, A.R., & Nakamura, Y. (1974). Immiscibility in late-stage magmas of the Skaergaard intrusion. *Carnegie Institute of Washington Yearbook* **73**, 348-352.

McBirney, A. R. & Nicolas, A. (1997). The Skaergaard Layered Series. Part II. Magmatic flow and dynamic layering. *Journal of Petrology* **38**,569-580.

McDonald, A.M.; Cabri, L.J.; Rudashevsky, N.S.; Stanley, C.J.; Rudashevsky, V.N; Ross, K.C. (2008). Nielsenite, $PdCu_3$, a new platinum-group intermetallic mineral species from the Skaergaard intrusion, Greenland. *The Canadian Mineralogist* **46**, 709-716

McKenzie, D. (2011). Compaction and crystallization in magma chambers: towards a model of the Skaergaard Intrusion. *Journal of Petrology* **52**, 905-930.

Makovicky, E. (2002). Ternary and quaternary phase systems with PGE. In J.P. Cabri (ed.): *The geology, geochemistry, mineralogy and mineral beneficiation of platinum-group elements.* Montreal: Canadian Institute of Mining, Metallurgy and Petroleum, Montreal, p. 131-175.

Meurer, W.P. & Boudreau, A.E. (1998). Compaction of igneous cumulates part I: Geochemical consequences for cumulates and liquid fractionation trends. *The Journal of Geology* **106**, 281-292.

Meurer, W.P., Willmore, C.C. & Boudreau, A.E. (1999). Metal redistribution during fluid exsolution and migration in the Middle Banded series of the Stillwater Complex. *Lithos* **47**, 143-156.

Miller, J.D. & Andersen, J.C.O. (2002). Attributes of Skaergaard-Type PGE Reefs. In Boudreau, A. (ed.). *Extended abstracts, 9th internat. Platinum Conference*, 305-308.

Momme, P., Tegner, C., Brooks, C.K. & Keays, R.R. (2002). The behaviour of platinum-group elements in basalts from the East Greenland rifted margin. *Contributions to Mineralogy and Petrology* **143**, 133-153.

Naldrett, A.J. (2004). *Magmatic Sulphide Deposits: Geology, Geochemistry and Exploration*. Heidelberg: Springer Verlag, 728 pp.

Naldrett, A.J., 2011, Fundamentals of Magmatic Sulphide Deposits. *Reviews in Economic Geology* **17**, 1-50.

Namur, O., Humphreys, M.C.S. & Holness, M.B. (2014). Crystallization of interstitial liquid and latent heat buffering in solidifying gabbros: Skaergaard intrusion, Greenland. *Journal of Petrology* **55**, 1389-1427.

Naslund, H.R. (1984). The petrology of the Upper Border Series of the Skaergaard intrusion. *Journal of Petrology* **25**, 1-28.

Nielsen, T.F.D. (1978). Dike swarms of the Kangerdlugssuaq Area, East Greenland and their bearing on the opening of the North Atlantic in Tertiary. *Contributions to Mineralogy and Petrology* **67**, 63-78.

Nielsen, T.F.D. (2001). The palladium potential of the Skaergaard intrusion. *GEUS report* **2001/23**, 39 pp.

Nielsen, T.F.D. (2004a). The shape and volume of the Skaergaard Intrusion, Greenland: implications for mass balance and bulk composition. *Journal of Petrology* **45**, 507-530.

Nielsen, T.F.D. (2004b). Platinum, palladium and gold in the Layered Series of the Skaergaard intrusion. *GEUS report* **2004/47**, 39 pp.

Nielsen, T.F.D. (2013). Origin of the world-class PGE-Au mineralisation in the Skaergaard intrusion by bulk sulphide-saturation, accumulation, partial dissolution, and secondary reef formation. *Abstract EGU General Assembly 2013, Geophysical Research Abstracts* **15**, EGU2013-7879.

Nielsen, T.F.D. & Bernstein, S. (2009). Chemical stratigraphy of the Triple Group and mineralisation of the Skaergaard intrusion: insight in the crystallisation process. *AGU Fall meeting 2009, Abstract* **V21A**-1956.

Nielsen, T.F.D. & Brooks, C.K., (1995). Precious metals in magmas of East Greenland: Factors important to the mineralisation in the Skaergaard intrusion. *Economic Geology* **90**, 1911-1917.

Nielsen, T.F.D., Andersen, J.C.Ø. & Brooks, C.K. (2005). The Platinova Reef of the Skaergaard intrusion.In: Mungal, J.E (ed.) *Exploration for Platinum Group element deposits.* Ottawa: Mineralogical Association of Canada, Short Course **35**, 431-455.

Nielsen, T.F.D., Olsen, S.D. & Stensgaard, B.M. (2009). Developing a 3-D model for the Skaergaard intrusion in East Greenland: constraints on structure, mineralisation and petrogenetic models. *Geological Survey of Denmark and Greenland Bulletin* **17**, 61-64.

Rudashevsky, N.S., McDonald, A.M., Cabri, L.J., Nielsen, T.F.D., Stanley, C.J., Kretser, Y.L., & Rudashevsky, V.N. (2004). Skaergaardite, PdCu, a new platinum-group intermetallic mineral from the Skaergaard Intrusion, Greenland. *Mineralogical Magazine* **68**, 615-632.

Rudashevsky, N.V. Rudashevsky, V.N. Nielsen, T.F.D. & Shebanov, A.D. (2014) Au-Cu alloys and inter-metallides in Pd-Au ores of the Skaergaard massif. *Proceedings of the Russian Mineralogical Society* **143(4)**, 1-23.

Rudashevsky, N.S. Rudashevsky, V.N. & Nielsen, T.F.D. (2015). Intermetallides and alloys of copper and palladium in ores of the Skaergaard massif. *Proceedings of the Russian Mineralogical Society* **144(1)**, 30-53.

Salmonsen, L.P. & Tegner, C. (2013). Crystallization Sequence of the Upper Border Series of the Skaergaard Intrusion: Revised subdivision and implications for chamber-scale magma homogeneity. *Contributions to Mineralogy and Petrology* **165**, 1155-1171.

Salmonsen, L.-P., Tegner, C.; Barfod, G. H.; Lesher, C. E. (2014). Compositional differences between roof and floor rocks of the Skaergaard Intrusion. *Abstract EGU General Assembly 2014, Geophysical Research Abstracts* **16**, EUG2014-12525, Vienna

Sonnenthal, E. L. (1992). Geochemistry of dendritic anorthosites and associated pegmatites in the Skaergaard intrusion, East Greenland: Evidence for metasomatism by a chlorine-rich fluid. *Journal of Volcanology and Geothermal Research* **52**, 209-230.

Svennevig, K. & Guarnieri, P. (2012). From 3D mapping to 3D modelling: a case study from the Skaergaard intrusion, southern East Greenland. *Geological Survey of Denmark and Greenland Bulletin* **26**, 57-60.

Tegner, C., Thy, P., Holness, M.B., Jakobsen, J.K & Lesher, C.E. (2009). Differentiation and compaction in the Skaergaard Intrusion. *Journal of Petrology* **50**, 813-840.

Thy, P., Lesher, C.E. & Tegner, C. (2009).The Skaergaard liquid line of descent revisited. *Contributions to Mineralogy and Petrol*ogy **157**, 735-747.

Thy, P., Lesher, C.E., Nielsen, T.F.D. & Brooks, C.K. (2006). Experimental constraints on the Skaergaard liquid line of descent. *Lithos* **92**, 154-180.

Tomkins, A.G. (2007). Three mechanisms of ore remobilisation at the amphibolite facies Montauban Zn-Pb-Au-Ag deposit. *Mineralium Deposita* **42**, 627-637.

Tomkins, A.G., Pattison, D.R.M. & Frost, B.R. (2007). On the initiation of metamorphic sulfide anatexis. *Journal of Petrology* **48**, 511-535.

Tomkins, A.G., Frost, B.R. & Pattison, D.R.M. (2006). Arsenopyrite melting during metamorphism of sulfide ore deposits. *The Canadian Mineralogist* **44**, 1317-1334.

Toplis, M.J. & Carroll, M.R. (1995). An experimental study of the influence of oxygen fugacity on Fe-Ti oxide stability, phase relations, and mineral-melt equilibria in ferro-basaltic systems. *Journal of Petrology* **36**, 1137-1171.

Turner, P.A. (1990). Report of the 1989 field season, Skaergaard concession. 47 pp. (in archive of Danmarks og Grønlands Geologiske Undersøgelse, GRF. no. 20843, available on-line).

Veksler, I.V., Dorfman, A.M., Borisov, A.A., Wirth, R, & Dingwell, D.B. (2007). Liquid immiscibility and the evolution of basaltic magma. *Journal of Petrology* **48**, 2187-2210

Wager, L.R. & Brown, G.M. (1968). *Layered Igneous Rocks*. Edinburgh and London: Oliver and Boyd, 588pp.

Wager, L.R., & Deer, W.A. (1939). Geological investigations in East Greenland: Part III. The petrology of the Skaergaard Intrusion, Kangerdlugssuaq, East Greenland. *Meddelelser om Grønland* **105**, 352 pp.

Watts, Griffis & McOuat Limited (1991). 1990 Skaergaard project, Platinova/Corona concession, East Greenland. Exploration report, 55 pp. and appendices (in archive of the Geological Survey of Denmark and Greenland, GRF no. 20848, available on-line).

Wilson A, Chunnett G. 2006. Trace element and platinum group element distributions and the genesis of the Merensky Reef, Western Bushveld Complex, South Africa. *Journal of Petrology*. **47,** 2369-2403.

Wotzlau, J.-F., Bindeman, I.N., Schaltegger, U., Brooks, C.K. & Naslund, H.R. (2012). High-resolution insights into episodes of crystallization, hydrothermal alteration and remelting in the Skaergaard intrusive complex. *Earth and Planetary Science Letters* **355**, 199-212.

FIGURE CAPTIONS

Fig. 1: Map, cross section and subdivision of the Skaergaard intrusion. *Host rocks:* Light yellow: Precambrian basement (B) and grey: Palaeogene flood basalts (FB). A: Simplified map of Skaergaard intrusion with sample profiles and drill core collar positions. Fat black stippled line: mineralisation level in lower half of Triple Group (open symbols in glaciated areas and across the

sea). Red dots: drill core collars (Watts, Griffis & McOuat Ltd., 1991; Hanghøj, 2005). Drill cores mentioned in text are identified (examples: 89-06 as 06 and 90-22 as 22). Red line with perpendicular tick marks: Standard profile (Tegner *et al.,* 2009). Line of red dots: Bollingberg profile (Bollingberg 1995; Holness *et al.,* 2007). Red line with dots: Kilen profile (UBS, Salmonsen & Tegner, 2013). Red line with crosses: Skaergaard Peninsula MBS profile (Holness *et al.*, 2011). B: East-West cross section (after Nielsen, 2004) with subdivisions in Fig. 1C. In black and with symbols: Sea level (S.L.), topography, and geology. The yellow zone in upper MZ is the anomalous 100m of stratigraphy of the Triple Group hosting the Skaergaard mineralisation. C: Correlation of zones and subzones of the roof gabbros (UBS), wall gabbros (MBS, blue) and the Layered Series (see legend) with phase layering and cryptic mineral compositions. Fig. 1C after Salmonsen & Tegner (2013).

Fig. 2. Pd+Pt (blue), Au (yellow) and Cu (red) in A: continuous 25cm bulk rock profile up the mineralisation in drill core 90-22 from the centre of the intrusion (data in Bernstein & Nielsen, 2004 and Appendix 4), and at decreasing distance to the margin of the intrusion B: in 1-m average samples from drill core 90-17A located ~ 1150m from the western margin of the intrusion (Pd+Pt and Au data from Watts, Griffis *&* McOuat Ltd. (1991), and C: in 1-m average samples from margin drill core 90-23A located ~ 900m from the eastern margin of the intrusion. (NB: logarithmic scale, Pd+Pt and Au data from Watts, Griffis *&* McOuat Ltd. (1991), Cu concentrations from Andersen (1996)). Naming of peaks after Nielsen *et al.* (2005). Leucogabbro layers $L0_p$ -L2 are shaded grey (definition of $L0_p$ = petrography versus $L0_{f+d}$ = field and density in text and fig. 19). The comparison shows the relative delay in Au and Cu-peaks in drill core 90-22 in the centre of the mineralisation and the absence of intrusion-wide time correlation of mineralisation processes.

Fig.3: Density stratification in drill core 90-22 from the centre of the mineralization. Mineralisation levels are always within sections of gabbros with upward decreasing density. The correlation is the same across the intrusion irrespective of the number of developed mineralisation levels (see appendixes 1-3 and 5).

Fig. 4: Saucer structure of the mineralisation in the Triple Group. Mineralisation levels are always concordant with lithological layering because the mineralization formed in stratigraphic levels of mush in solidifying gabbro. The model was first presented by Andersen *et al*. (1998) and is based on the data given in Nielsen (2001) and in Appendices 1-3 and 5.

Fig. 5: Backscatter images of the petrographic relations of FeTi-oxides in Middle Zone gabbros and the floor mineralization. Abbreviations: Plag: plagioclase, Ol: olivine, Cpx: clinopyroxene,

TiMt: titanomagnetite, Ilm: ilmenite, Ap: apatite, S: Cu sulphide, Sym: symplectite (plag-ol-cpx), P1: liquidus paragenesis of bulk liquid, P2; subliquidus mush melt paragenesis, MZ: Middle Zone. Stratigraphic position, sample number, and length of scale bar are given for each image. A: Interstitial P2 TiMt and Ilm and Ol rim in contact with to resorbed primocrystic P1 Plag and Cpx (lower MZ, GM 84-362, 100µm); B: Resorbed primocrystic P1 Cpx surrounded by late P2 Ol in contact with embayed and resorbed primocrystic P1 Plag (lower MZ. GM 84-360, 100µm); C: Interstitial P2 FeTi-oxides (TiMt and Ilm) surrounded by a rim of P2 Ol followed by P2 Sym (similar to Holness *et al.* (2011), Pd5 peak, 90-22 1033.25, 100µm); D: P2 TiMt and Sym in fracture in primocrystic P1 Plag. P2 Plag of P2 Sym is more An rich (lighter colour). The P2 vein cuts older mineralised fractures in P1 Plag (Pd5 peak, 90-22 1033.25, 100µm); E: anhedral P2 FeTi-oxide grain with euhedral P2 apatite crystals. The FeTi-oxides are surrounded by an incomplete rim of P2 Ol, P1 Cpx is partly re-crystallised. S: droplets of Cu-rich sulphide melt (Pd5 peak, 90-22 1033.25, 100µm); F: Ilmenite hosted, rounded, crystallised, silicate melt inclusion (see Godel *et al.*, 2014) composed dominantly of hydrous ferromagnesian silicates. The irregular rim shows crystallization of host ilmenite from the original melt droplet (upper MZ, GGU 360018, 10µm).

Fig. 6: Mosaic image (cross polarized light) of gabbro in Pd5 peak of the mineralisation in drill core 90-22, sample 1033.25. The gabbro has a fabric defined by alignment of plagioclase and is characterized by large proportions of interstitial FeTi-oxides (Ti-magnetite and ilmenite). The enlargement illustrates: Paragenesis 1 consisting mainly of (commonly partially resorbed) plagioclase and clinopyroxene, and paragenesis 2 crystallised from Fe-rich immiscible melt and comprising: Ti-Magnetite and ilmenite (black, see also Fig. 5c for same area of the thin section), Sym: symplectites, RP: recrystatalized clinopyroxene, and R: olivine and orthopyroxene rims.

Fig. 7: Selected backscatter images of precious metal minerals of the floor mineralization. Abbreviations: ilm: ilmenite; ch: chalcocite; bn: bornite; sk: skaergaardite (PdCu); cpx: clinopyroxene; AuCu: tertra auricupride; BT: biotite; chl: chlorite; ZV: zvyagintsevite; P2: subliquid paragenesis of mush melt. Mineralisation levels, sample number, and length of scale bar are indicated. A: Cu-sulphide droplet (bn and ch) hosted in ilmenite (lower Pd5, 90-24 1059, 30µm); B: Cu-sulphide droplet (ch and bn) with euhedral crystal of skaergaardite (sk, Pd2b, 90-18 978, 10µm); C: anhedral matrix grain of Cu-sulphide (ch and bn) with euhedral skaergaardite crystal (sk, lower Pd5, 90-24 1059m, 30µm); D: anhedral grain of skaergaardite (sk) attached to P2 bn, cpx, and ilm (Pd1, 90-24 1022, 10µm); E: rounded grain of Skaergaardite (sk) with attached bn (lower Pd5, 90-24 1059, 10µm); F: euhedral crystal of tetra-auricupride (AuCu) attached to small grain of matrix bn (Pd3, BS 0304, 10µm); G: Two anhedral grains of AuCu

attached to matrix ilm and BT (Pd3, 90-24 1018 (error in core number in BSI), 10μm), H: anhedral grain of ZV attached to matrix chlorite (chl) (Pd5, 90-23A 807 10μm), I: euhedral crystal of ZV in anhedral matrix bn (upper Pd5, 90-23A 806, 10μm), J: droplet of precious metal melt enclosed in anhedral ch grain. Note meniscus separating the precious metal droplet from the surrounding Cu-sulphide. The precious metal droplet is composed of skaergaardite (sk, white) and chalcosite (Pd4a, 90-24 1045, 10μm); K: grain of anhedral skaergaardite (sk, white) and bornite (bn, gray) crystallised from a droplet of precious metal melt (Pd3a, 90-24 1034, 10μm).

Fig. 8. A: Whole rock Cu (ppm) in UBS, MBS and LS plotted against remaining fraction of melt (*F*). Note small differences in the timing of the Cu-peaks in the three series. Data in Appendix 6.

Fig. 9. Pd and Pt in a grab sample profile through the Layered Series (LS) of the Skaergaard intrusion (Bollingberg profile in Nielsen (2004)). Note that the x-axes are logarithmic. A: Pd +Pt in LS and B: Pd/Pt. Mineralisation in yellow interval. Pd+Pt decreases up to LZc (green interval), increases in PGE and Pd/Pt between F= 0.45-0.3 (purple interval) are caused by local mush melt sulphide saturation and accumulation of Pd and Pt (see Fig. 10.), and in the low PGE zone (red interval, data in Appendix 11) both Pd+Pt and Pd/Pt are low.

Fig. 10. Pd/Pt versus (Pd+Pt) in LS. A: Samples above and below the mineralisation. Samples have, apart from one with very low Pt (1 ppb), a maximum Pd/Pt determined by Pd/Pt = 3+(Pd/10) reflecting the initial Pd/Pt of 3 in Skaergaard bulk liquid and the maximum solubility of Pt of ~10 in basaltic melt. B: The mineralisation level is dominated by trend 1 with strongly increasing (Pd+Pt) and low Pd/Pt and trend 2 with strongly increasing Pd/Pt and decreasing (Pd+Pt). Neither trend is similar to trends above or below the mineralisation. The grey field is defined by compositions of samples below and above the mineralisation in the floor of the intrusion in Fig. 10a. See text for further details.

Fig. 11: Pt (blue), Pd (green), Au (yellow) in ppb and Cu (red) in ppm at the Cu peak in hand sample profiles in: A: UBS and B: MBS. UBS shows, at the given sample resolution, no stratigraphic separation of precious metals and Cu. MBS shows a stratigraphic separation in accordance with distribution coefficients with Pd >Pt>Au>Cu.

Fig. 12. Log-log plot of Cu versus Pt (A), Pd (B) and Au (C) in the 25cm bulk sample profile, drill core 90-22 (Bernstein & Nielsen, 2004, Appendix 4). Blue: Suite 1, samples from Pd6-Pd3 and Pd2a and b levels (main PGE mineralisation levels); green: Suite 2 from the intervals between Pd3, Pd2 and Pd1 peaks; yellow: Suite 3 from the Pd1 and overlying Au levels; and red: Suite 4, Cu-rich samples above the Au-rich levels (Suite 3). The four suites point to a "common

composition" with ~13 ppb Pd, ~1.3 ppb Pt and ~10 ppb Au, suggesting a Pd/Pt ~10, Au/Pd ~0.8, and Au/Pt ~8.

Fig. 13. A: Total PGE (Pd+Pt, blue) and Pd/Pt (green) versus depth in continuous 25cm bulk rock profile, core 90-22 (260 samples). Pd peaks indicated. Note the comparatively low and increasing Pd/Pt across the main PGE peak (Pd5), except for the local maxima at 1033 - 1032m and the high Pd/Pt in level Pd4b. B: Simplified stratigraphic variation in Pd/Pt showing the averages for each Pd level (yellow, averages of samples with Pd+Pt > than half peak concentration), and in red the average Pd/Pt in the lower part of all Pd levels (from peak value to lower cut off at half peak concentration). Pd5 is distinct in having low Pd/Pt. The division between lower PGE mineralisation (LPGEM, Pd5 and Pd4), the upper PGE mineralisation (UPGEM, Pd3 to Pd1) and upper Au mineralisation (UAuM) is shown to the right.

Fig. 14: Core compositions of liquidus plagioclase (electron microprobe data) versus normative bulk rock plagioclase (CIPW) in roof, walls and floor of the intrusion. Squares: LS, dots: UBS, dominos: MBS. Purple: below mineralisation, green: Pd-rich mineralisation (Pd5 to Pd1), orange: Au mineralisation level, and red: above mineralisation. Light blue squares: compositions of liquid plagioclase correlated to normative plagioclase composition of bulk liquid (as in Nielsen *et al.,* 2009). Big symbols: data first shown in this investigation, small symbols (LS) previously published data (Appendix 8).

Fig. 15. Variation in ratios between Pd, Pt, and Au during solidification of the Skaergaard intrusion and the formation of the floor mineralisation. Based on the mass balance model of Nielsen (2004) and on data in Appendix 7. Abbreviations: BL: bulk liquid of Skaergaard intrusion; LZb,: bulk liquid at LZa/b boundary; LZc: bulk liquid at LZc/Mz boundary; Z. bulk liquid at base of low-PGE-zone (see text and Appendix 11); BM: bulk liquid at mineralisation level; M: average of mineralisation (drill core 90-22); A: average of all melt remaining after the mineralisation event. A: Line of liquid descent and comparisons to: grey field: Geickie Plateau Formation Lavas (Momme *et al*., 2002) and chill of Skaergaard-like dyke E (Nielsen & Brooks, 1995); open circles: gabbros of LZa and b; filled squares: gabbros of LZc and MZ below low-PGE-zone; and open triangles: low-PGE-zone (data; drill core 90-10 in Watts, Griffis & McOuat Ltd (1991), and Appendix 11). B and C: abbreviations as in Fig. 15A; open triangle and l-PGE-z: average low-PGE-zone; red open dots: averages of mineralisation in drill core intersects on basis of assay data (Watts, Griffis & McOuat Ltd., 1991); orange dot: common composition (CC, based on these diagrams, see text); and large circle: common composition (CC, based on Fig. 12). The

correlation l-PGE-z— Z— CC is during late loss of Au and minor Pt pivoted (shown by arrow) into the correlation A— BM—M (in red).

Fig. 16: $TiMt_{24}$ (red) and Ilm_{24} (purple) up through core 90-22 (25cm continuous bulk profile). L-layers (grey) are also shown. $TiMt_{24}$ is calculated as normative titanomagnetite with 24 wt% TiO_2. Note the 6-7m repetitive ilmenite-rich levels with no clear distribution relative to leucogabbro layers L0-L2.The Ilm_{24} peaks have a TiMt24/Ilm24 ratio of 0.6, near that of the experimental liquidus paragenesis of Thy *et al.* (2006). The Ilm_{24} peaks are taken to reflect levels of ilmenite nucleation in melt of a composition similar to bulk melt (see text).

Fig. 17. Co-variation of $TiMt_{24}/Ilm_{24}$ and normative plagioclase/pyroxene across the mineralisation. The data can be described using three endmembers: (1) pyroxene rich P1 (bulk liquid) cumulate with little P2 (immiscible Fe-rich melt: $TiMt_{24}$); (2) plagioclase-rich P1 cumulate with little P2 ($TiMt_{24}$) contribution; and (3) plagioclase-poor gabbro rich in P2 $TiMt_{24}$. Modes of the host rocks of the main PGE mineralisation (Pd5, blue) and the gold-rich rocks (yellow) in the upper part of the mineralisation are identified. Data in Appendix 4. See text for further detail.

Fig. 18. Macrolayers of the mineralisation defined using the ratio of normative plagioclase (an+ab) and pyroxene (cpx+opx). Melagabbro is defined by plag/px < 0.7 and leucogabbro by plag/px>1. Data in Appendix 4. Three out of four macrolayers are 13-14m thick, whereas the last is 20m and may represent the combination of two macrolayers (see text). Transition between macrolayers is defined by gabbro with low concentrations of FeTi-oxides (see details in Fig. 22).

Fig. 19. Details of the transition between macrolayers ML0 and ML1 (Fig. 18) and the relationship the Pd5 mineralisation level (based on data in Appendix 4). Buff coloured: L0 as seen in the field and overlapping with $L0_{d+f}$ as identified in density logs as a low density layer). This layer is poor in FeTi-oxides and has a plag/px ~1. Yellow: gabbros below ($L0_p$) with a high proportion of P1 plagioclase (high plag/px), but also high to very high P2 $TiMt_{24}$ (see also figs. 5 and 6). $L0_p$ is composed of accumulated (floating) P1 primocryst plagioclase in a matrix rich in P2 $TiMt_{24}$ and hosts most of mineralisation level Pd5. $L0_{d+f}$ lies above the leucograbbro top of macrolayer ML0 ($L0_p$) and is the transition into the pyroxene-rich base of the overlying ML1 macrolayer. L0 as seen in the field is not comparable with L1 to L3 of the Triple Group.

Fig. 20. Margin to centre variation in shape and size of Pd5 peak. Depth in drill cores standardised to Pd5 peak = 0m. See text for further comments. Data from Turner (1990) and Watts, Griffis *&* McOuat Ltd. (1991).

Fig. 21. Stratigraphic variation in Pd+Pt (ppb), $TiMt_{24}/ilm_{24}$, Pd/Pt, and Cu (ppm) from low-PGE-zone to the base of Pd5 peak, including Pd6 (termed the "subzone" by Holwell & Keays (2014)). The increase in Pd/Pt is continuous, whereas Pd+Pt increases in steps. Cu and Pd+Pt show no correlation. Constant or decreasing Pd+Pt correlates with elevated or increasing $TiMt_{24}/Ilm_{24}$, caused by the deposition of precious metals hosted in sulphide droplets from mush melt (at local $F \sim 0.18$, Table 4) and subsequent re-dissolution (d) of these droplets of sulphide melt in stratigraphic concentrations of the Fe-rich immiscible residual of the same mush melt (immiscibility at $F \sim 0.1$, Table 4). The model is developed and illustrated in Fig. 22.

Fig. 22. Five snapshots of the solidification and mineralisation process in "proto-macrolayer" ML0 (Fig. 18) hosting the Pd5 mineralisation level. Stage 1: Liquidus plagioclase (P1 paragenesis) floated to form leucogabbro (LG, see stage 2), while pyroxene and minor liquidus FeTi-oxides (P1 paragenesis) sank to form pyroxene-rich cumulates (MG = melanogabbro), creating a intermediate layer of melt-rich mush (hypothetical proportions indicated in column to the left). The transition zones between macrolayers (TZ) are gabbros poor in FeTi-oxides (e.g. $L0_{f+d}$). Stage 2: evolved mush liquid reached sulphide-saturation (at local $F \sim 0.18$) and sulphide droplets formed (yellow). They were disseminated throughout the mush melt (see text). Stage 3: mush liquid reached the two-silicate liquid field (at local $F \sim 0.1$), Si-rich immiscible melt started to rize and left behind a mush melt continuously enriched in Fe. Unprotected sulphide droplets started to dissolve (green dots) as the solubility of S increased. Stage 4: Si-rich immiscible melt was lost continuously from the mush, Fe-rich melts accumulated between gabbro and leucogabbro, FeTi-oxides crystallised in significant proportions (as in $L0_p$), protected sulphide droplets (yellow) were preserved while unprotected droplets dissolved and were reduced to droplets of precious metals melts (green). Stage 5: Leaving the liquidus paragenesis of the immiscible Fe-rich mush melt behind, the residual silicate melt and the accompanying free volatile phase were driven upwards by compaction (see section on UAuM). They carried along incompatible elements including gold (Au) into the overlying and lesser crystallised macrolayers. Black markings on left side of column: Levels enriched in P1 ilmenite. Modification of the primary composition of the sulphide melt is modelled in Figure 15.

Fig. 23. Pd+Pt and $TiMt_{24}$ variation up through the mineralisation (data in Appendix 4). $TiMt_{24}$ mimics the variation in Pd+Pt with Pd levels (blue arrows) above the corresponding $TiMt_{24}$ enrichment levels (red arrows) at Pd4, Pd3b and a, the near perfect stratigraphic correlation in Pd2b and a, and perfect correlation in Pd1. Concentration of Pd+Pt and crystallisation of $TiMt_{24}$ (P2 paragenesis) coincide in Pd1. The gradual change in relative timing demonstrates the

development to sulphide saturation of immiscible Fe-rich liquid at $F \sim 0.1$ (see text for explanation).

Fig. 24. Cu in hand samples collected at 1m intervals in drill core 90-24 (Andersen, 1996) equivalent samples from the standard profile (Tegner *et al*., 2009; Salmonsen & Tegner, 2013). Core 90-24 is parallel and similar to drill core 90-22 in Fig. 2a. Correlation based on calculated *F* (see Appendix 6). The interval at 1000-1010 m in drill core 90-24, for which no Cu data are available, is the Au peak in core 90-24. In the more detailed sampling of core 90-24, Cu does not form a single well-defined enrichment level as suggested by the standard profile. Cu shows stratigraphic accumulation similar to Pd levels of the precious metal mineralisation and sulphide-saturation at local $F \sim 0.18$ in mush melt (see text for further explanations and Table 4 for timing of sulphide-saturation in Skaergaard melt). Cu anomalies in Upper MZ and lowest UZa do not reflect bulk liquid sulphide saturation.

Figure 25: Mineralogical traces of *in situ* fractionation in Skaergaard gabbro. A: LZb sample GM 84254: apatite crystals accumulated on grain boundaries with little trace of the mush melt (FeTi + ol) from which they crystallised. B: Trace of reaction between liquidus titanomagnetite and accumulated immiscible Si-rich liquid roof gabbro (sample SK08 163). The magnetite of the exsolved spinel is replaced by fayalite and hedenbergite. Note the remains of magnetite in the central part of the former spinel. Quartz plus magnetite reacts to fayalite and hedenbergite. Abbreviations: Cpx: clinopyroxene; plag: plagioclase; ap: apatite; FeTi: FeTi-oxides including Ti-magnetite and ilmenite; ol: olivine; and ilm: ilmenite.

Fig. 26. Model for the redistribution of Fe, and sulphide melt with dissolved precious metals in the Skaergaard intrusion at LPEGM time. Lower left: Abbreviations for melts and parageneses A: section of the Skaergaard intrusion after Nielsen (2004, sketch is not to scale). Cross hatched: host rocks, grey: crystallised gabbro, dotted: mush zone between liquidus and solidus. White: remaining bulk liquid. UBS: Upper Border Series (roof), MBS: Marginal Border Series (walls) and LS: layered Series (floor). B: Complementary sections in roof and floor mush, combinations of parageneses and melts in sections in lower middle of figure. In the roof, formation of Fe-rich mush melt causes an overturn between evolved bulk melt with sulphide droplets and Fe-rich melt that sinks into stronger convective flow (indicated by the increasing size of arrows to the right of the columns). Fe-rich melt with load of partially solidified sulphide droplets (protected or under dissolution) is transported to floor mush (see text for further explanation) to be redistributed in the floor as illustrated in Fig. 22.

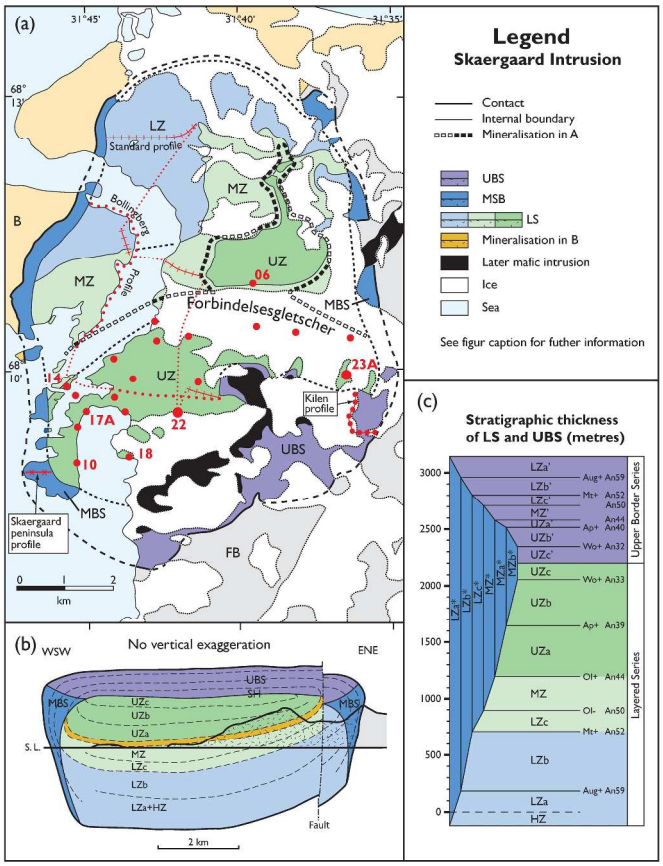

297x420mm (300 x 300 DPI)

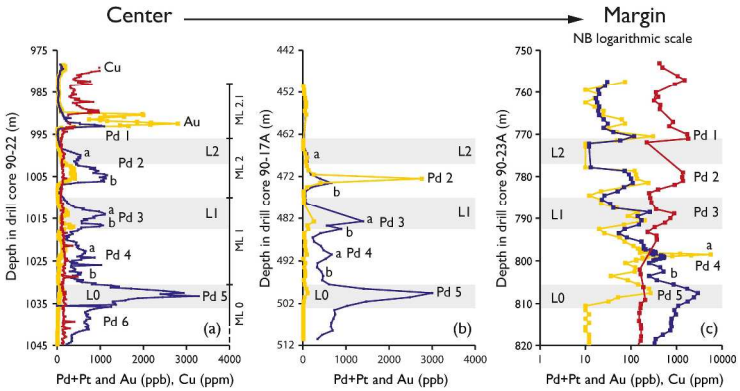

297x420mm (300 x 300 DPI)

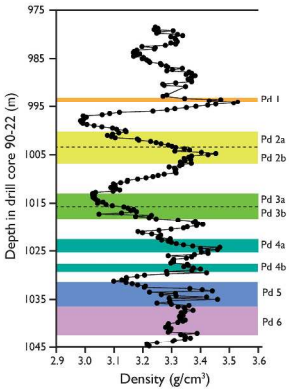

297x420mm (300 x 300 DPI)

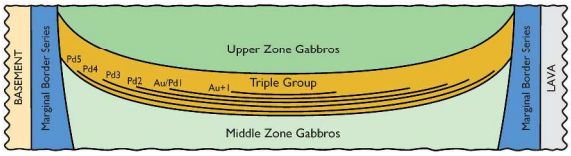

NOT TO SCALE

297x420mm (300 x 300 DPI)

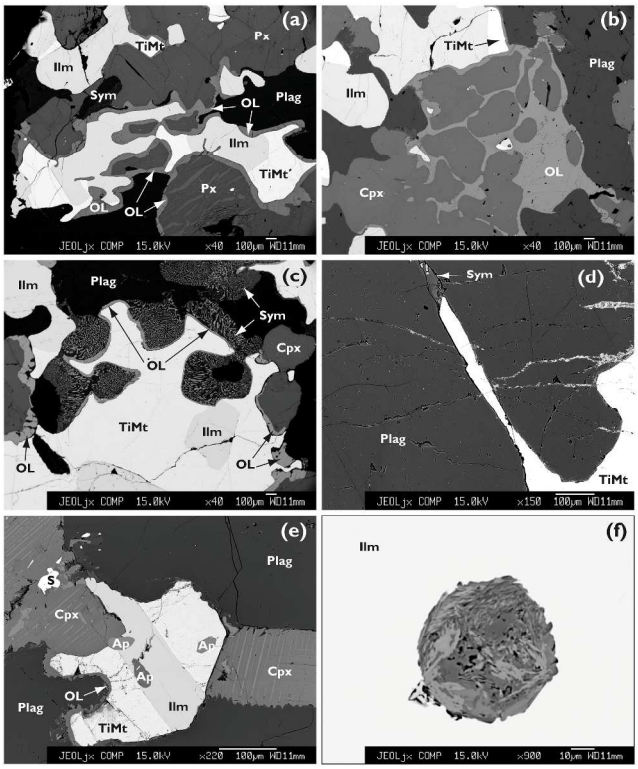

297x420mm (300 x 300 DPI)

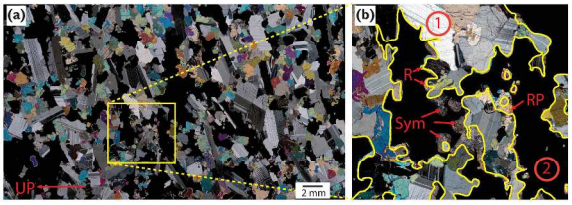

297x420mm (300 x 300 DPI)

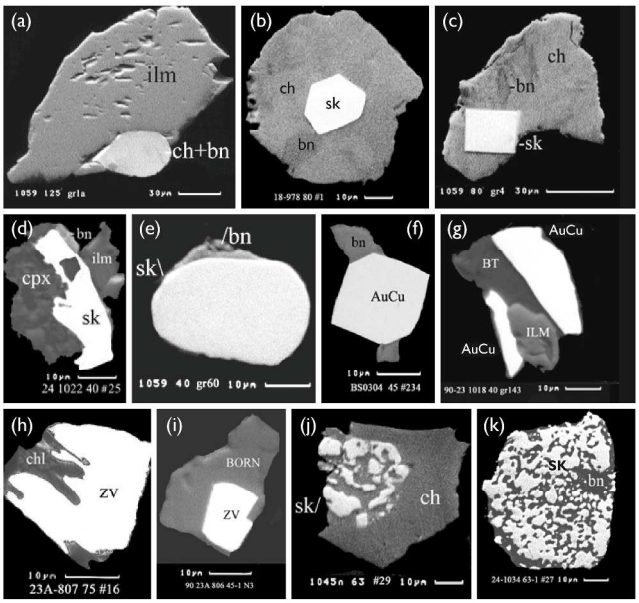

297x420mm (300 x 300 DPI)

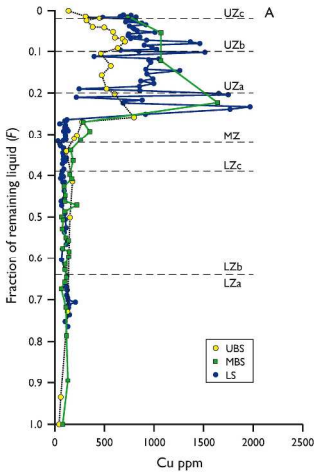

297x420mm (300 x 300 DPI)

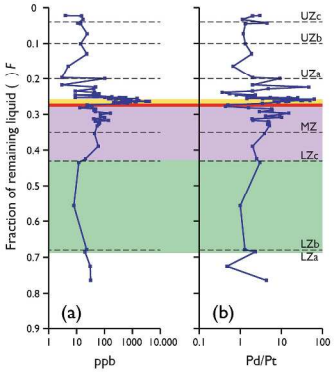

297x420mm (300 x 300 DPI)

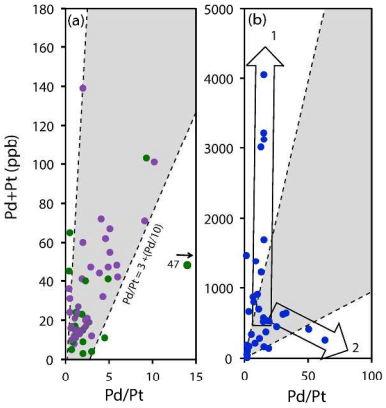

297x420mm (300 x 300 DPI)

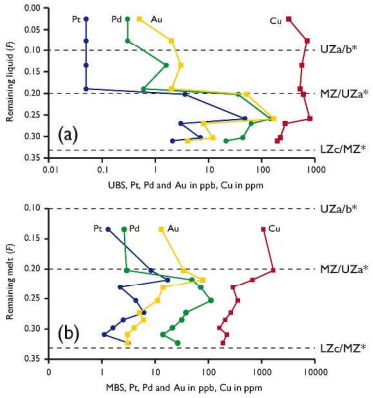

297x420mm (300 x 300 DPI)

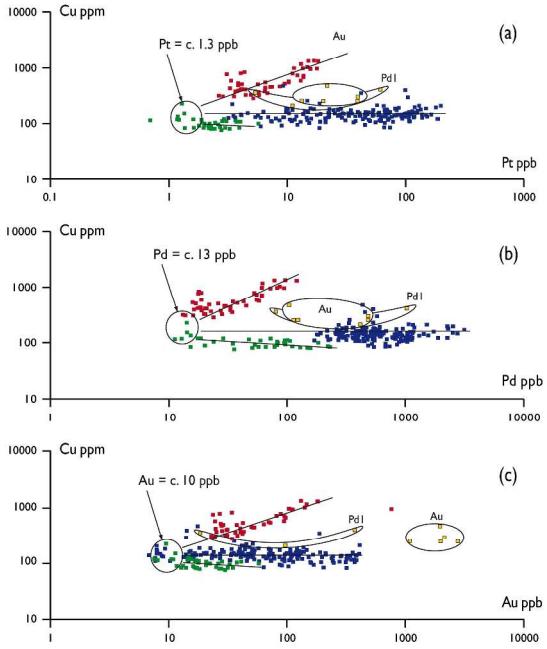

297x420mm (300 x 300 DPI)

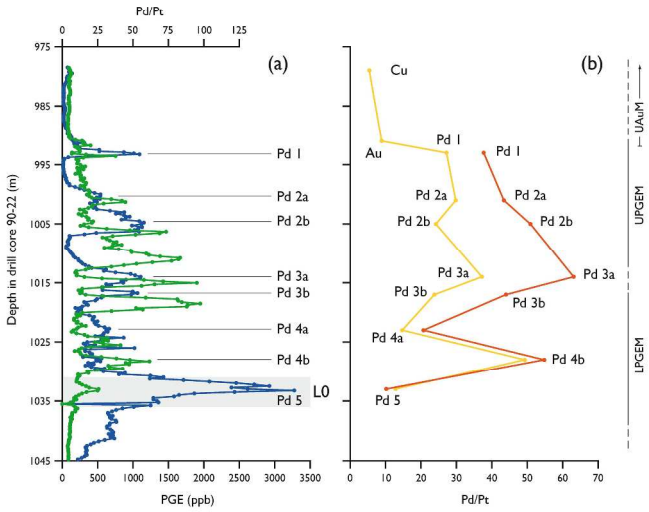

297x420mm (300 x 300 DPI)

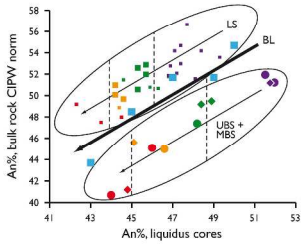

297x420mm (300 x 300 DPI)

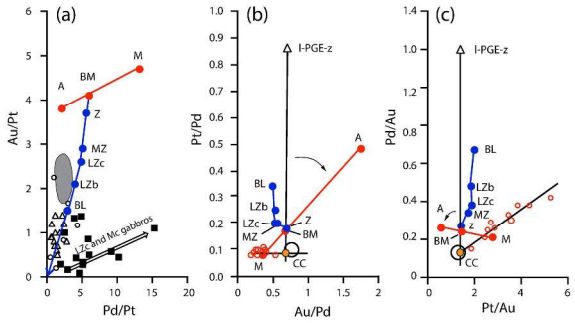

297x420mm (300 x 300 DPI)

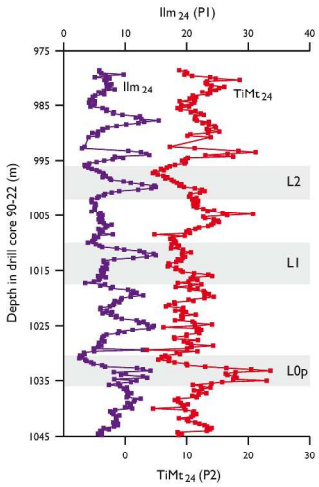

297x420mm (300 x 300 DPI)

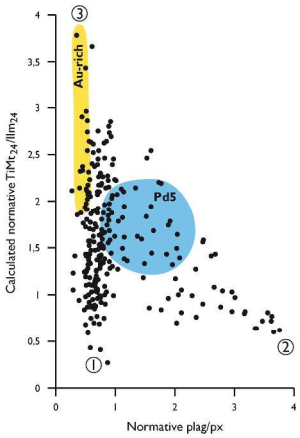

297x420mm (300 x 300 DPI)

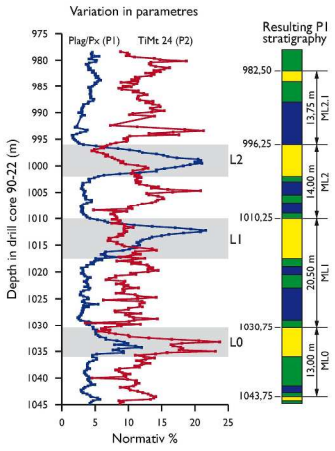

297x420mm (300 x 300 DPI)

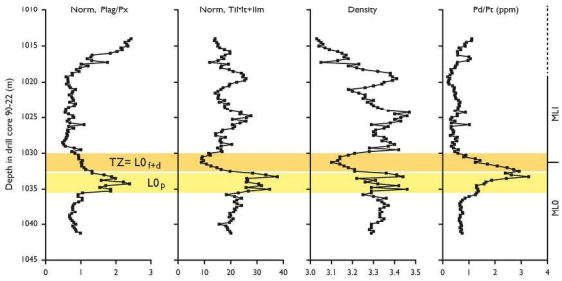

209x148mm (300 x 300 DPI)

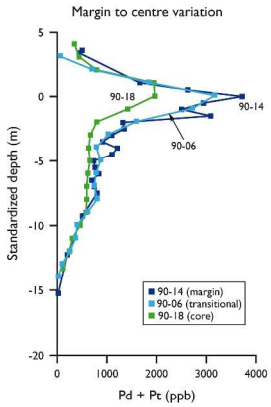

297x420mm (300 x 300 DPI)

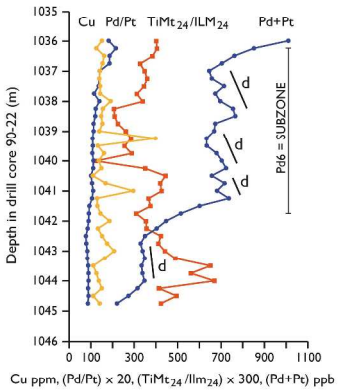

297x420mm (300 x 300 DPI)

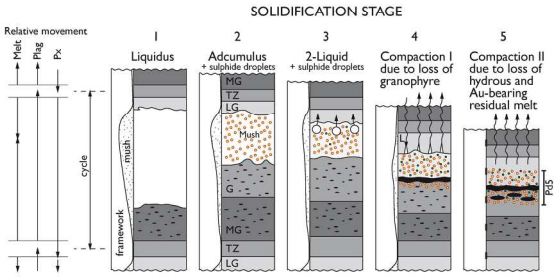

209x148mm (300 x 300 DPI)

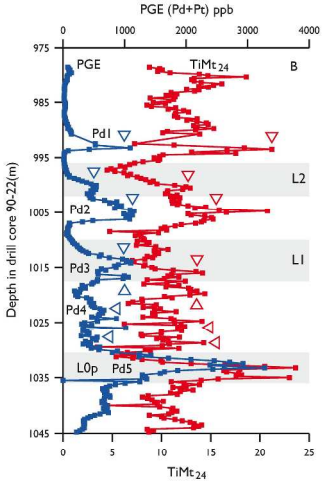

297x420mm (300 x 300 DPI)

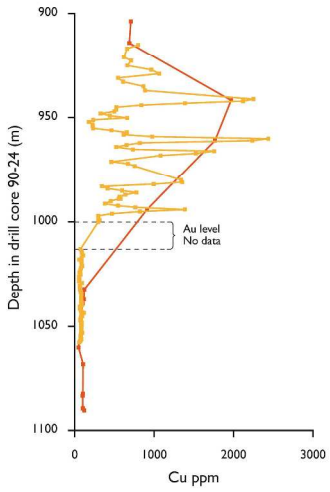

297x420mm (300 x 300 DPI)

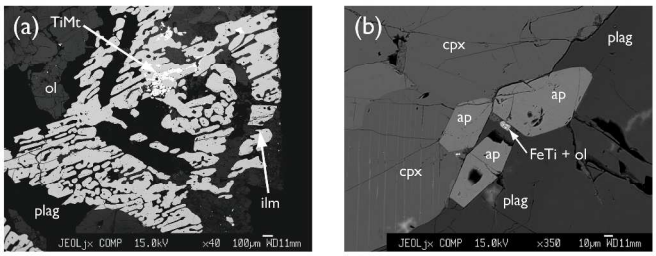

297x420mm (300 x 300 DPI)

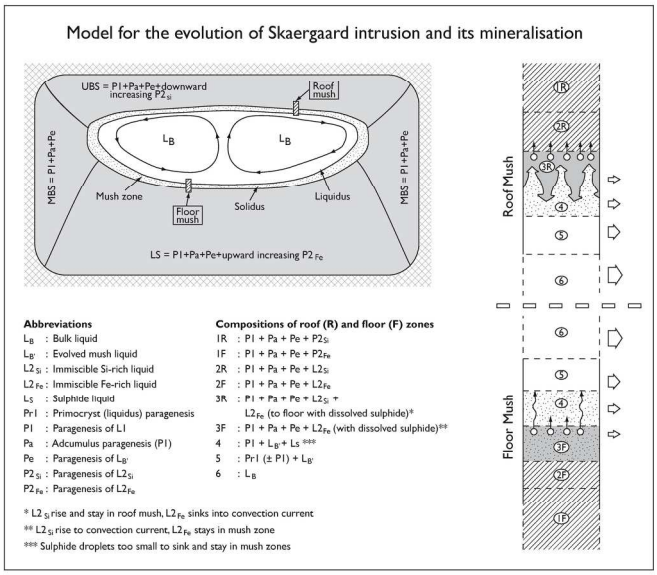

209x176mm (300 x 300 DPI)

*Table 1: Summary of stratigraphic separation between tops of leucogabbro layers betweeen L-layers and Pd-levels, and Pd-levels (meters)**

	L0-L1	L1-L2	L2-L3	L1-Pd5
average separation	20.0	14.0	67.0	21.4
screened av. separation**	20.0	15.0	67.0	21.3
deviation	0.0	1.0	0.0	0.1

	Pd5-Pd4b	Pd4b-Pd4a	Pd4a-Pd3b	Pd3b-Pd3a	Pd3a-Pd2b	Pd2b-Pd2a	Pd2a-Pd1
average separation	4.9	4.5	6.3	3.2	8.0	3.9	8.1
screened av. separation**	4.9	4.4	6.3	3.3	8.0	3.9	8.1
deviation	0.0	0.1	0.0	0.1	0.0	0.0	0.0

*Data from Appendices 1 and 3.

** excluding the 4 intersect with largest deviation from the average

Table 2: Cu, Pt, Pd and Au concentrations in Upper Border Series (UBS) and Marginal Border Series (MBS)

sample	zone	equi. zone	Relative to mineralisation	m	F	Cu ppm	Pt ppb	Pd ppb	Au ppb	PGE (Pt+Pd) ppb	Pd/Pt	Pd/Au	Au/Pt
MBS													
SP 28	Uza*	Uza	above	578.7	0.13	1069	1.3	2.6	13.0	3.9	2.0	0.2	10.0
SP 27	MZ*	MZ	Cu-peak	564.2	0.21	1642	8.3	2.9	34.0	11.2	0.3	0.1	4.1
SP 26	MZ*	MZ	Au-Pt-peak	551.0	0.22	665	17.1	48.8	78.0	65.9	2.9	0.6	4.6
SP 25	MZ*	MZ	secondary Pd	539.4	0.24	286	2.2	71.2	14.0	73.4	32.4	5.1	6.4
SP 24	MZ*	MZ	Pd-peak	521.0	0.26	353	4.3	111.0	11.0	115.3	25.8	10.1	2.6
SP 23	MZ*	MZ	below	504.6	0.28	261	6.1	37.6	5.0	43.7	6.2	7.5	0.8
SP 22	MZ*	MZ	below	494.0	0.29	205	2.5	31.4	6.0	33.9	12.6	5.2	2.4
SP 21	MZ*	MZ	below	483.2	0.30	159	1.6	21.0	4.0	22.6	12.6	5.3	2.5
SP 20	MZ*	MZ	below	474.0	0.31	220	1.1	13.9	3.0	15.0	12.6	4.6	2.7
SP 19	MZ*	MZ	below	462.6	0.32	185	3.1	26.3	3.0	29.4	8.5	8.8	1.0
UBS													
SK08-147	gamma	Uza	above	180	0.03	320	*<0.1*	*<0.5*	<1	<0.5	void	void	void
SK08-153	gamma	Uza	above	270	0.08	707	*<0.1*	*<0.5*	2	<0.5	void	void	void
SK08-156	gamma	Uza	above	354	0.14	564	*<0.1*	1.6	3	>1.6	void	>0.53	void
SK08-158	gamma	Uza	above	413	0.19	521	*<0.1*	0.5	2	>0.5	void	>0.25	void
SK08-159	gamma	Uza	top of Cu, Au?	425	0.20	603	3.6	32.5	52	36.1	9.03	0.63	14.4
SK08-161	beta	MZ	Cu, Au	471	0.26	798	48.1	96.8	167	144.9	2.01	0.58	3.5
SK08-162	beta	MZ	Pd-zone	479	0.27	274	3.0	60	8.0	63	20.00	7.50	2.7
SK08-163	beta	MZ	below	502	0.30	222	7.0	36.9	12.0	43.9	5.27	3.08	1.7
SK08-197	beta	MZ	Below	507	0.31	195	19.1	9.1	2.1	28.2	0.48	4.33	0.1

Analytical techniques in text.

Table 3: Comparison between Pd, Pt and Au in contemporaneous basaltic liquids with mg# <0.5

	Giekie Pl. Form. lava*	Giekie Pl. Form. lava*	Giekie Pl. Form. lava*	SK-like dyke chill**	SK bulk this work***
GGU #	436009	435641	436068	361045	Fig. 15
Mg#	0.46	0.43	0.49	0.38	0.45
Pt ppb	4.5	3.7	5.8	10	8.5
Pd ppb	10.4	12.9	13.2	27	24.6
Au ppb	12.4	7.8	9.7	21	12.6
Pd+Pt	14.89	16.60	18.96	37.00	37.20
Pd/Pt	2.32	3.49	2.29	2.70	1.95
Au/Pd	1.19	0.60	0.73	0.78	0.51
Au/Pt	2.76	2.11	1.68	2.10	1.48

* Geikie Plateau Formation lava, Momme *et al*. (2002)
** Skaergaard like dyke E, Nielsen & Brooks (1995)
*** Based on mass proportions in Nielsen (2004a)
Mg#: MgO/(MgO+FeO) wt% with all Fe as FeO.

Table 4: Relative timing of processes in Skaergaard melt

	Sample or source	Estimated and modelled F	Observed or interpolated An%	Requirred proportion of crystallistion to achieve sulphide saturation	Requirred proportion of crystallistion to achieve silicate-silicate liquid immiscibility
UZc/UZb	Thy et al. (2009)	0.02	33	Saturated	emulsion
UZb/UZa	Thy et al. (2009)	0.10	39	Saturated	emulsion
Silicate-silicate immiscibility	Jakobsen etal. (2005)	0.10**	39	Saturated	emulsion
Suplhide- sat., bulk liquid*	Calculated (this work)	0.18	43	Saturated	0.44
Cu anomaly wall	SP-27	0.21	45	0.05	0.54
UZa/MZ	Thy et al. (2009)	0.21	45	0.17	0.57
Cu anomaly floor	This work	0.25	44	0.24	0.60
Cu anomaly roof	SK08-161	0.26	47	0.27	0.62
Au, floor	This work	0.25	44	0.27	0.60
Au wall	SP-26	0.23	42-45***	0.14	0.57
Au roof	SK08-161	0.26	47	0.27	0.62
Pd5, floor	This work	0.26	45	0.27	0.62
Pd anomaly wall	SP-24	0.27	49	0.30	0.63
Pd anomaly roof (high Pd/Pt)	SK08-162	0.27	48	0.30	0.63
low PGE zone	This work	0.28-0.26	48	0.34	0.66
MZ/LZc	Thy et al. (2009)	0.33	50	0.46	0.71
LZc/LZb	Thy et al. (2009)	0.40	53	0.53	0.75
LZb/LZa	Thy et al. (2009)	0.67	60	0.72	0.85

* based on increase in Pd/Pt from 6 to 9 in LLB for Pd, Pt and Au (Fig. 15b and c). At Pt=-10 ppb, Pd/Pt in bulk was 60 and increase to Pd/Pt = 9 requirres crystallisation of c. 1/3 of the remaining bulk melt.

** Based on Jakobsen et al. (2005). Jakobsen et al. (2011) suggest silicate-silicate immiscibility at LZc, but as argued in text, the LZc immisciility is referred to processes in mush liquid.

*** Namur et al. (2014)

Table 5: Summary of mineralisation mineralogy in the Pd1 level and in the upper Au mineralisation (UAuM) in core 90-24.

UAuM paragenesis: Sample 90-22 1018	
A single paragenesis formed later than and along grain boundaries between rock forming minerals (Rudashevsky et al., 2014)	
Tetra auricupride (92 vol%):	AuCu
(Au,Cu) alloy:	(Au,Cu)
(Cu,Au) alloy:	(Cu,Au)
Auricupride:	Cu_3Au
Melnoite:	$(Ni,Pd)Te_2$
Unnamed telluride 1:	$Cu,Fe)_9Te_2S_3$
Unnamed telluride 2:	$(Cu,Fe)_6TeS_2$
Unnamed telluride 3:	$Pd_3(Cu,Fe)6Te_2S_3$
Orcelite:	$Ni_{5-x}As_2$
Kotulskite:	PdTe
Sperrylite	$PtAs_2$
Acantite	Ag_2S
Pd1 paragenesis: Sample 90-24 1022	
Two parageneses are identified from relationships between grains. The early is related to interstitial sulphide melt formation, the second to late re-equilibration environment in the presence of a free volatile phase (Rudashevsky et al., 2015)	
Skaergaardite (61 vol%):	(Pd, Au)Cu
Tetra-auricupride (27 vol%):	(Au,Pd)Cu
(Au,Cu,Pd) alloys (7.7 vol%):	(Au,Cu,Pd)
Nielsenite:	$(Pd,Au,Pt)Cu_3$
Zvyagintsevite:	$Pd_3(Pb,Bi)$
Keithconnite:	$Pd_3(Te,Sn,Pb)$
(Pd,Cu,Sn) alloy:	(Pd,Cu,Sn
Vasilite:	$(Pd,Cu)_{17}S_6$
Kotulskite:	PdTe
Auricupride:	$(Au,Pd)Cu_3$
Native Ag	Ag
Telargpalite	$(Pd,Ag)_3(Te,Bi,Pd)$,
Unnamed $(Pd,Ag)_2Te$	Unnamed $(Pd,Ag)_2Te$
Unnamed Pd_3Ag_2S	Unnamed Pd_3Ag_2S